Elucidating Texture and Grain Morphology Contributions to the Micromechanical Response of Additively Manufactured Inconel 625

Reilly J. Knox[a], Robert Carson[b], Matthew Rolchigo[c], Katherine S. Shanks[d], James Belak[b], Darren C. Pagan[a]

[a] *Materials Science and Engineering, The Pennsylvania State University*
[b] *Computational Engineering Division, Lawrence Livermore National Laboratory*
[c] *Computing and Computational Sciences Directorate, Oak Ridge National Laboratory*
[d] *Cornell High Energy Synchrotron Source, Cornell University*

Abstract

Microstructural variation of additively manufactured (AM) metal components in comparison to wrought counterparts makes certification for critical applications a challenge. Microscale simulations leveraging modern computational tools may be used to supplement testing of AM microstructures, thus accelerating certification by reducing the number of experiments needed. However, as micromechanical response is closely tied to critical properties like fatigue-life and fracture, utilization of these simulations with macroscale experimental data alone is insufficient. One means to attain microscale experimental data is *in situ* diffraction data collected from synchrotron X-ray sources. In this work, such data were collected during *in situ* compression of AM Inconel 625 superalloy. Interpretation of experimental results was assisted by massive (8M element) complementary micromechanical simulations performed on sets of virtual microstructures generated using cellular automata. Together, micromechanical data from diffraction experiments and simulations were used to probe the effects of texture, morphology, and directional strength-to-stiffness on micromechanical response. Though fiber-averaged directional strength-to-stiffness ratios were expected to dominate, micromechanical response was instead significantly modulated by grain neighborhood effects driven by texture and morphology. The findings emphasize the importance of high-fidelity microstructural representation for property prediction of AM metals.

1. Introduction

Simulations are a powerful tool for accelerating understanding of additive manufacturing (AM) processes and certification of AM products, with mechanical modeling often comprising a crucial downstream component of such approaches. However, for confidence in mechanical response predictions, capturing macroscopic yield behavior does not guarantee accuracy of the model at the mesoscale (micromechanical response), as a homogenized macroscopic response does not correspond to a unique mesoscopic deformation path [1, 2, 3, 4]. Since micromechanical response is closely tied to other performance-critical macroscopic responses like fatigue-life and fracture, simulating the effects of microstructure requires complementary microscale experiments that capture the complexity of deformation of AM microstructures, particularly *within bulk polycrystals*.

The advantages of a combined simulation and microscale testing approach have been shown, for example, by Quey et al., who combined *ex situ* electron backscatter diffraction (EBSD) and finite element simulations to probe grain orientation fragmentation in a hot-deformed Al alloy [5]. The need for such an approach has also been demonstrated, for example, by Sangid et al., who tested crystal plasticity (CP) models using experimental strain fields measured from *ex situ* digital image correlation and EBSD [1]. In comparing the results of these models to experiment and one another across length scales, comparisons worsened from near-perfect at the macroscale to poor at the slip system scale.

Confidence in capturing the full-field effects of microstructure may be increased by capturing the evolution of quantities that reflect these effects, such as micromechanical data collected from *in situ* diffraction experiments [6]. Efstathiou et al. [7] and Wielewski et al. [8] used lattice strain data from *in situ* high-energy X-ray diffraction experiments to determine the single-crystal elastic constants of Ti alloys, while Pagan et al. used slip system strength evolution extracted from *in situ* far-field high-energy X-ray diffraction microscopy of Ti-7Al to calibrate a CP model for the material [9]. Wong et al. combined *in situ* high-energy X-ray diffraction measurements, a crystal-based finite element model, and a virtual diffractometer framework to investigate grain-scale stress and deformation heterogeneity during cyclic loading of Cu [10]. Carson et al. used a similar methodology to develop intragrain diffraction-based and mechanics-based deformation heterogeneity metrics [11]. As information regarding both the macroscopic and mesoscopic deformation states is embedded in these data, they may be used to support detailed modeling of the effects of

microstructure on mechanical response.

This demand for complementary modeling and experiment is especially great for alloys fabricated via AM, as these materials often have complex microstructures and mechanical properties resulting from nonequilibrium processes evolving under large temperature gradients, rapid solidification, and thermal cycling. Murr et al., for example, observed a significant increase in room temperature elongation compared to the wrought form for Ni superalloy Inconel 625 (IN625) with columnar precipitate architecture fabricated via electron beam melting [12]. Zhang et al. leveraged thermal cycling and rapid solidification to produce Ti-Cu alloys with both fine equiaxed prior-β grains and ultrafine eutectoid lamella displaying high yield strength and uniform elongation compared to conventional alloys [13]. Similarly, Zhu et al. formed dense internally-twinned nanoprecipitates in laser powder bed fusion (LPBF) of Ti alloy Beta-C not typically observed in traditionally manufactured Ti alloys, resulting in unusually high tensile strength while retaining suitable ductility [14]. Studies have also revealed substantial intragranular misorientation in AM metals, indicating a high density of geometrically necessary dislocations that act as powerful barriers to dislocation motion [15].

In this work, a series of *in situ* high-energy X-ray diffraction experiments were performed on AM IN625 during uniaxial compression. From the measured diffraction data, micromechanical response (lattice strain) was tracked as a function of macroscopic load state for subsets of grains belonging to different crystallographic fibers. Complementary crystal plasticity finite element method (CPFEM) simulations were performed on virtual microstructures to help interpret experimental findings and further understand sources of variation in micromechanical response between microstructures despite equivalent macroscopic stress-strain states.

This work is organized as follows: materials and methods are discussed in Section 2, including experimental data collection, generation of virtual microstructures, simulation methodology, X-ray data processing, and simulation data post-processing. The results of experiment and simulation are presented in Section 3 and findings thereof discussed in Section 4, with attention given to the roles of texture, morphology, and elastic and plastic anisotropy on micromechanical response. Rather than being dominated by directional strength-to-stiffness ratios, micromechanical response was instead found to be modulated by grain neighborhood effects driven by texture and morphology. Concluding remarks are made

in Section 5, emphasizing the importance of high-fidelity microstructural representation for AM property prediction. Note that tildes over variables (e.g., $\tilde{\sigma}$, $\tilde{\varepsilon}$) indicate macroscopic quantities.

2. Materials and Methods

2.1. Material

Specimens for *in situ* compression were extracted from an AM IN625 bridge structure, an LPBF build (AMB2018-01) from the National Institute of Standards and Technology's (NIST) AM benchmark test series [16]. The bridge structure was built in a modified EOS M270 testbed using the build parameters in Table 1, with a schematic of the build shown in Fig. 1 [16, 17, 18]. The location on the bridge structure from which the samples were extracted is marked. Information regarding build geometry and feedstock material may be found in Levine et al. [16, 17]. A brick specimen geometry of $1.0 \times 1.0 \times 2.5$ mm was chosen to prevent buckling during compression, with the long dimension chosen as the loading direction (LD). A total of 9 specimens were extracted from the indicated leg 7 (L7, see Fig. 1), with their long dimension (and LD) coinciding with the build direction (BD) of the bridge structure. Specimens were extracted from the same vertical position in the leg, but different locations from throughout the leg cross-section with varying distance from the leg edges. A subset of specimens (3) were used for method development, while the remaining 6 (labeled E1-6 for "experimental") were used for data collection.

EBSD data are presented in Fig. 2 for a 0.5×0.5 mm region from the interior of neighboring leg L1 (Fig. 1, equivalent in size and build conditions to L7). Inverse pole figure coloring of the data with respect to BD indicates that the microstructure consists predominantly of large $\langle 110 \rangle$-oriented columnar grains with tracks of finer $\langle 100 \rangle$-oriented material between them. These observations are corroborated by the orientation inverse pole figure (IPF) and orientation pole figures (PFs) from a representative specimen (E1) shown in Fig. 3. Note that all IPFs in this work are with respect to BD/LD, all PFs show BD/LD out-of-plane, and both are presented in multiples of uniform density (MUD). IPFs and PFs for all experimental specimens are shown and contrasted in Appendix A. Though the orientation distributions vary between specimens, all were found to have high $\{220\}$ and $\{200\}$ densities along BD. This indicates common $\langle 110 \rangle$ and $\langle 100 \rangle$ fiber texture components along this direction, corresponding to large volume fractions of grains oriented

with ⟨110⟩ or ⟨100⟩ along BD. The relative strengths of these fiber texture components along BD vary by specimen (see Appendix A). In contrast, all specimens showed an absence of {111} density along BD, indicating few grains oriented with ⟨111⟩ along BD. Despite these commonalities, texture variations between specimens and large grain sizes relative to the beam size resulted in probed volumes not acting as representative volumes [19] for the bulk LPBF build (discussed further below). Some of these variations may be attributed to differences in microstructure near and away from the edges of L7 (Fig. 1). These builds are known to have a stronger cube texture near the leg edges [20], which may contribute to the experimental texture variability.

2.2. Data Collection

X-ray measurements were collected at room temperature at the Forming and Shaping Technology (FAST/ID3A) beamline at the Cornell High Energy Synchrotron Source (CHESS). A 0.5×0.5 mm beam with energy 61.332 keV (Yb K-edge) was used in a transmission geometry with two Dexela 2923 area detectors in a vertically stacked arrangement. The detectors were positioned 675 mm behind the specimens so that the fourth Debye-Scherrer ring, {311}, was fully captured on the detectors. A schematic of this setup is provided in Fig. 4. The detector geometry with respect to sample position was calibrated prior to testing using a CeO_2 powder reference acquired from NIST.

PF data for each specimen, such as those shown in Fig. 3, were collected every 0.25° over a 180° rotation in ω (Fig. 4) prior to mechanical testing. The 6 specimens were distributed among 3 target engineering strain rates (10^{-4}, 10^{-3}, and $10^{-2}\,s^{-1}$) for *in situ* compression to assess strain rate-dependence. Each sample was loaded at its prescribed strain rate in the RAMS2 load frame [21] with tungsten platens to approximately 6% engineering strain, then unloaded at the same rate. Macromechanical data and polycrystalline diffraction data were collected continuously and simultaneously at 5 Hz.

Macroscopic engineering stresses ($\tilde{\sigma}$) and strains ($\tilde{\varepsilon}$) were determined from a load cell in the load path and measured crosshead displacements, respectively. Machine compliance comprised a significant fraction of measured crosshead displacements. As such, both linear and nonlinear machine compliance effects were corrected using a procedure modified from Kalidindi et al. [22] such that stiffness in the elastic regime for each sample was consistent with its texture-dependent directional stiffness.

To compute the texture-dependent directional stiffness of each specimen, 50000 orientations were sampled from its orientation distribution function, computed from its PF data using MTEX [23]. For each orientation, an arbitrary uniaxial stress tensor was applied along LD (z) in the sample frame, then converted to the crystal frame. The anisotropic form of Hooke's law was applied with IN625 single-crystal elastic constants from Wang et al. [24] to calculate the corresponding elastic strain tensor in the crystal frame, which was then converted to the sample frame. The directional stiffness of that orientation is the ratio $\sigma_{zz}/\varepsilon^{e}_{zz}$ of the normal stress (σ_{zz}) and elastic strain (ε^{e}_{zz}) components along LD. The texture-dependent directional stiffness of the specimen is then the mean over all sampled orientations.

2.3. ExaAM Modeling

The Exascale Additive Manufacturing Project (ExaAM), part of the U.S. Department of Energy's Exascale Computing Project (ECP), is a multi-stage, multi-physics simulation workflow leveraging exascale computing for high-fidelity modeling of process-structure-property-performance relationships in metal AM parts [25, 26]. This work utilizes two components of the workflow: the cellular automata (CA) code ExaCA and the CPFEM code ExaConstit. These components are used together to fully encompass process-microstructure-property relations [25, 27].

Previous efforts have demonstrated the ability of the workflow to successfully predict macroscopic stress-strain behavior [26]. However, the effects of microstructure on micromechanical response, tied to other macroscopic responses such as fracture and fatigue-life, have not previously been investigated using this workflow. To this end, ExaConstit simulations were performed using 48 CPUs and GPUs on the Summit supercomputer at Oak Ridge National Laboratory's Leadership Computing Facility and 32 CPUs and GPUs on the Lassen compute platform at Lawrence Livermore National Laboratory (LLNL). Simulations were performed on 2 sets of simulated microstructures extracted from larger voxelized columnar microstructures generated with ExaCA. These microstructures and simulations are described in further detail below.

2.3.1. Microstructure Generation

ExaCA [28, 29] is an open-source CA-based model used to generate explicit microstructures. The model uses melt pool and thermal history data to simulate dendritic grain

structure evolution during alloy solidification [28, 30]. Inhomogeneity in the liquid is incorporated by marking a fraction of the liquid cells as potential nucleation sites using a heterogeneous nucleation density. Nucleation undercoolings are sampled from a prescribed Gaussian distribution and assigned to each site. If a liquid cell cools to its assigned undercooling, nucleation occurs and the cell becomes active, receiving a grain ID and an octahedral grain envelope. The solidification front is tracked using active cells, and each envelope is tracked independently. At each time step, the envelopes of active cells whose temperatures have dropped below the liquidus are independently incremented using an interfacial response function to emulate sub-grain dendritic growth physics. In ExaCA, this function is a third-order polynomial function of local undercooling fit to experimental dendrite growth velocities. The code leverages the Gandin-Rappaz decentered octahedron algorithm [31] to handle the conversion of active cell-adjacent liquid cells into new active cells, each inheriting the grain ID of the parent active cell. For a more detailed description of ExaCA, see [29].

The first series of ExaConstit simulations used microstructures generated using melt pool shapes and thermal histories in ExaCA predicted by upstream components of the ExaAM workflow [26, 32]. Heat transfer simulations were performed on representative odd/even layers of the full $5 \times 5\,\text{mm}$ L7 cross-section (Fig. 1) using AdditiveFOAM [33], an open-source heat and mass transfer software for AM simulations. Temperature data for the central $1 \times 1\,\text{mm}$ region were interpolated to the CA cell size. ExaCA repeated the representative odd/even layer data for that region with layers offset by $20\,\mu\text{m}$ to simulate a $1 \times 1 \times 1\,\text{mm}$ cube. 125 ExaCA simulations were performed with different permutations of AdditiveFOAM data and ExaCA nucleation parameters. $0.5 \times 0.5 \times 0.5\,\text{mm}$ cubes were then taken from each set of ExaCA voxel data for use in ExaConstit simulations. This methodology is illustrated in Fig. 5.

From these 125 microstructures, the 4 microstructures with simulated macroscopic stress-strain responses in closest agreement with previous bulk experiments [26] were chosen. These simulated microstructures will be referred to as the F ("full workflow") microstructures and labeled F1 through F4. The bounds from which these $0.5 \times 0.5 \times 0.5\,\text{mm}$ cubes were taken from the larger $1 \times 1 \times 1\,\text{mm}$ cubes are given in Table 2, in addition to other details of the microstructure labeling scheme. The z bounds $[0.5, 1]$ were used because the top halves of the $1 \times 1 \times 1\,\text{mm}$ cubes were observed to be representative of the microstructure the rest of the way up L7.

One of these simulated microstructures (F1) is shown in Fig. 6A with IPF-z coloring of the grains. Note the tendency toward colors near the $\langle 111 \rangle$ corner of the IPF triangle (blue) and away from the $\langle 110 \rangle$ (green) and $\langle 100 \rangle$ (red) corners, indicating a tendency toward orientations of the $\langle 111 \rangle$ fiber rather than the $\langle 110 \rangle$ and $\langle 100 \rangle$ fibers as observed in experiment. This is corroborated by the IPF and PFs for F1 in Fig. 7A, representative of the F microstructures. All F microstructures showed a $\langle 111 \rangle$ fiber texture component along BD, notably paired with a lack of $\{220\}$ and $\{200\}$ density along BD. This contrasts with the $\langle 110 \rangle$ and $\langle 100 \rangle$ fiber texture components and lack of $\{111\}$ density along BD characteristic of experiment.

The second series of simulations used microstructures from ExaCA with melt pool shapes and thermal histories modified based on phenomenological descriptions of the build process. For these, AdditiveFOAM data for single lines were instead translated, mirrored, and rotated to form odd/even layer raster patterns. These microstructures were generated in pursuit of textures better matching experiment, to be discussed later. Four cubic $0.5 \times 0.5 \times 0.5\,\text{mm}$ simulated microstructures were taken from voxel data generated using a spot size of $D4\sigma = 80\,\mu\text{m}$ and a nucleation density of $7.5 \times 10^{14}\ \text{m}^{-3}$. This contrasts with the F microstructures, for which only one microstructure each was taken from 4 sets of voxel data. These will be referred to as the P ("phenomenological") microstructures and labeled P1-4 per the bounds of the ExaCA voxel data from which each was taken (described in Table 2).

One of these simulated microstructures (P1) is shown in Fig. 6B with IPF-z coloring of the grains. Note the strong tendency toward the $\langle 110 \rangle$ (green) and $\langle 100 \rangle$ (red) corners of the IPF triangle and away from the $\langle 111 \rangle$ (blue) corner, better matching experiment (Fig. 3). Also note the similarities with the EBSD data in Fig. 2, as both show large $\langle 110 \rangle$-oriented columnar grains with tracks of finer $\langle 100 \rangle$-oriented material between them. The corresponding IPF and PFs in Fig. 7B, representative of the P microstructures, show orientation distributions with the $\langle 110 \rangle$ and $\langle 100 \rangle$ fiber texture components and lack of $\{111\}$ density along BD characteristic of experiment. Note that these pole figures show maxima > 3 MUD, in excess of the 3 MUD color scale upper bound. This bound was chosen to use the same color scale for all PFs while retaining suitable contrast to accentuate the features of interest.

A third series of simulations was also run to help separate the effects of texture and morphology. These microstructures were the same as the P microstructures, but with grain

orientations reassigned to eliminate the texture observed for the P microstructures described above. The responses of these microstructures are reported and discussed in Appendix B.

2.3.2. Micromechanical Modeling

ExaConstit [34] is an open-source nonlinear quasi-static implicit solid mechanics code application for probing deformation of polycrystalline materials [25, 26, 35], with crystal plasticity models supported through the ExaCMech library [25, 35, 36]. In brief, the code solves for the balance of linear momentum using typical solid mechanics FEM discretizations of the weak form combined with strain kinematics and crystal-scale constitutive responses [25, 26]. In this work, a large-strain single-crystal elasto-viscoplastic model was used with elastic and plastic deformations described by multiplicative decomposition of the deformation gradient. Anisotropic elasticity was incorporated [6, 11], with power law slip kinetics linking the resolved shear stress τ^α for each slip system α with its slip system shearing rate $\dot{\gamma}^\alpha$:

$$\dot{\gamma}^\alpha = \dot{\gamma}_0 \left| \frac{\tau^\alpha}{g^\alpha} \right|^{1/m} \operatorname{sgn}\left(\tau^\alpha\right) \ , \tag{1}$$

where m is the rate exponent, $\dot{\gamma}_0$ the base shearing rate, and g^α the critical resolved shear stress (CRSS) for α [37, 6, 11]. A standard linear Voce hardening law was used with isotropic slip system hardening:

$$\dot{g}^\alpha = h_0 \left(\frac{g_\mathrm{s} - g^\alpha}{g_\mathrm{s} - g_0} \right) \sum_\beta \dot{\gamma}^\beta \ , \tag{2}$$

where $\dot{g}^\alpha$ is the hardening rate for α, h_0 the hardening coefficient for all α, g_0 the initial CRSS for all α, and g_s the saturation CRSS for all α [6, 37, 11].

The microstructure cubes extracted from the ExaCA voxel data were meshed using ExaConstit's built-in mesh generator, producing suitable 8 million-element MFEM meshes [38]. In the subsequent ExaConstit simulations, every quadrature point in an element was modeled as a face-centered cubic crystal with a single orientation. Lower-length scale phases [24, 39, 40, 41, 42, 43, 44] implicitly affect the hardening behavior but are not explicitly modeled. The model described above was used with single-crystal elastic constants from Wang et al. [24], with the remainder of the requisite micromechanical parameter set tabulated in Table 3. Each microstructure was compressed at the 3 experimental strain rates (10^{-4}, 10^{-3}, and $10^{-2}\,\mathrm{s}^{-1}$) to approximately 5% engineering strain over 81 time steps. The same optimized time-stepping sequence was used for all simulations, scaled accordingly by factors of 10 for different strain rates.

2.4. X-ray Data Processing

All raw diffraction data were processed using the HEXRD library [45] to extract PF and micromechanical data (lattice strains). An interpolation-based polar remapping was used to map each diffraction image onto a rectilinear grid with ordinates of 2θ (twice the Bragg angle) and azimuthal angle η. As these were polycrystalline diffraction measurements, lattice plane behaviors are considered in an averaged sense across some suitable subset of grains (grains with orientations within a prescribed tolerance of a crystallographic fiber). Here, orientation averaging is achieved by integration over η across a prescribed azimuthal bin, resulting in a 1D line profile of intensity vs. 2θ for the bin. For pole figure data, 5° bins were used with η centers every 5°. For *in situ* compression data, 10° bins were used with η centers at 90° and 270°, corresponding to BD/LD (applied compression). The bins for the latter case are illustrated in Fig. 4. A suitable number (based on strain rate) of corresponding line profiles for serial images were summed for each specimen to reduce the volume of data used in subsequent fitting procedures.

Peak centers were determined by fitting pseudo-Voigt functions to these integrated line profiles. For PF data, peak centers and their intensities for each bin (line profile) were mapped to PFs using their angular coordinates $(2\theta, \eta, \omega)$. For *in situ* data, lattice strains ε_{hkl} were the micromechanical quantity of interest. These strains are defined for a family of lattice planes $\{hkl\}$ based on the change in interplanar spacing d_{hkl}:

$$\varepsilon_{hkl} = \frac{d_{hkl} - d^0_{hkl}}{d^0_{hkl}} \ , \tag{3}$$

where d_{hkl} and d^0_{hkl} are the current and initial interplanar spacings, respectively. In this work, d^0_{hkl} was taken as the lattice plane spacing at the start of loading. The interplanar spacing of lattice plane family $\{hkl\}$ is related to its corresponding Bragg angle θ_{hkl} (peak center) by way of Bragg's law:

$$\lambda = 2d_{hkl} \sin\theta_{hkl} \ , \tag{4}$$

where λ is the X-ray wavelength. Lattice strains may then be computed directly from changes in peak positions between load steps as:

$$\varepsilon_{hkl} = \frac{\sin\theta^0_{hkl}}{\sin\theta_{hkl}} - 1 \ , \tag{5}$$

where θ_{hkl} and θ^0_{hkl} are the current and initial peak centers, respectively. As only subsets of grains (as subdivided by θ_{hkl} and azimuthal bin) contribute to the measured lattice

strains, these strains offer insight into microscale elastic and plastic anisotropy. That is, ε_{111} describes the average micromechanical evolution along LD for only the subset of grains with $\langle 111 \rangle$ oriented within 5° of BD/LD, ε_{200} the subset of grains with $\langle 100 \rangle$ oriented within 5° of BD/LD, and so on.

2.5. Simulation Data Post-Processing

To compare simulation to experiment, PF data and lattice strains were extracted from each simulated microstructure. Element orientations, elastic strain tensors $\boldsymbol{\varepsilon}^{\mathrm{e}}$, and volumes are among the many quantities evolved at each time step. PFs were generated from each simulated microstructure by using its initial spatial distribution of orientations to calculate its orientation distribution function in MTEX [23]. To calculate lattice strains at each time step, the elements belonging to the $\{hkl\}$ fiber were identified as those having orientations that align the $\{hkl\}$ plane normal within 5° of BD/LD (equivalent to the 10° azimuthal bins used for X-ray data processing). For each element i belonging to the $\{hkl\}$ fiber, its lattice strain $\varepsilon_{i,hkl}$ was computed by projecting its elastic strain tensor along the lattice plane normal $\mathbf{n}_{hkl}$:

$$\varepsilon_{i,hkl} = \boldsymbol{\varepsilon}_i^{\mathrm{e}} : (\mathbf{n}_{hkl} \otimes \mathbf{n}_{hkl}) \ . \tag{6}$$

Finally, the volume fraction v_i of each element was used in a weighted average to calculate the average lattice strain of the fiber ε_{hkl}:

$$\varepsilon_{hkl} = \sum_{i \in \{hkl\}} v_i \varepsilon_{i,hkl} \ . \tag{7}$$

Also of interest for the virtual microstructures were their directional strength-to-stiffness ratios r_{hkl}, associated with the average yield behavior for grains in each fiber. These ratios were calculated using the approach by Wong and Dawson [46]. In this approach, the directional strength of a crystallographic fiber is defined as the average steady-state Taylor factor M_{hkl} of grains in the fiber in fully developed plasticity, computed as:

$$M_{hkl} = \left(\frac{\sum_\alpha |\dot{\gamma}^\alpha|}{D^{\mathrm{p}}_{\mathrm{eff}}} \right)_{hkl} \ , \tag{8}$$

where the subscript hkl denotes a volume-weighted average over elements in the fiber as in Eq. 7 and $D^{\mathrm{p}}_{\mathrm{eff}}$ is the effective plastic deformation rate. The plastic deformation rate $\mathbf{D}^{\mathrm{p}}$ is computed as:

$$\mathbf{D}^{\mathrm{p}} = \sum_\alpha \dot{\gamma}^\alpha \ \mathrm{sym} \left(\mathbf{s}^\alpha \otimes \mathbf{m}^\alpha \right) \ , \tag{9}$$

where $\mathbf{s}^\alpha$ and $\mathbf{m}^\alpha$ are the slip direction and slip plane normal, respectively, of each slip system α [6, 37, 11]. $D^{\mathrm{p}}_{\mathrm{eff}}$ is then:

$$D^{\mathrm{p}}_{\mathrm{eff}} = \sqrt{\tfrac{2}{3}\left(\mathbf{D}^{\mathrm{p}} : \mathbf{D}^{\mathrm{p}}\right)}\,. \tag{10}$$

The directional stiffness of each fiber is defined as its elastic stiffness prior to yielding, as this value may vary post-yield due to load redistribution between grains in different fibers. Since the simulated loading was uniaxial compression, the directional stiffness E_{hkl} of the fiber is the ratio of the Cauchy stress and elastic strain components along the loading direction. For loading along z as in experiment, E_{hkl} is given by:

$$E_{hkl} = \left(\frac{\sigma_{zz}}{\varepsilon^{\mathrm{e}}_{zz}}\right)_{hkl}\,, \tag{11}$$

where hkl again denotes a volume-weighted average over elements in the fiber. The directional strength-to-stiffness ratio r_{hkl} of the fiber is then:

$$r_{hkl} = \frac{M_{hkl}}{E_{hkl}}\,. \tag{12}$$

As defined, this quantity incorporates information regarding both elastic (directional stiffness) and plastic (directional strength) anisotropy. The quantities ε_{hkl}, M_{hkl}, and E_{hkl} were calculated *in situ* during each ExaConstit simulation. Equivalent Python scripts for *ex situ* calculations are available in the ExaConstit repository [34].

3. Results

3.1. Experiment

The macroscopic stress-strain responses of the 6 experimental specimens are shown in Fig. 8, with colors and line styles denoting different strain rates and specimens, respectively. Though the curves are clustered, they are not ordered by strain rate as might be expected [47, 48], to be discussed later. Figures 9A-F show the evolution of lattice strains along LD with macroscopic strain for the 4 subsets of grains (grains belonging to specific crystallographic fibers) considered for each specimen. The order of yielding and magnitude at yield were consistent across all samples for 3 of the 4 lattice strains - ε_{220} (red), then ε_{311} (orange), then ε_{200} (purple). Yield ordering is related to - but not solely determined by - the directional strength-to-stiffness ratio of each crystallographic fiber [46], explored later using simulation data. This contrasts with the highly variable response of the remaining lattice strain, ε_{111}

(blue). Its magnitude relative to the other lattice strains is inconsistent, being the smallest for E1, E2, and E6 (Figs. 9A,B,F), falling between ε_{220} and ε_{311} for E3 and E5 (Figs. 9C,E) and crossing below ε_{220} at large macroscopic strain for the latter, and falling between ε_{311} and ε_{200} for E4 (Fig. 9D). Whereas other lattice strains exclusively harden, ε_{111} initially displays a unique "softening" behavior after yield in some specimens, especially apparent in E1, E2, and E4 (Figs. 9A,B,D). For E2 and E4, this pronounced softening is followed by hardening comparable to the other lattice strains. Note that these anomalous ε_{111} behaviors show no dependence on the strain rate at which each sample was tested.

3.2. Simulations

The macroscopic stress-strain responses of the 4 F microstructures simulated at the 3 experimental strain rates are shown in Fig. 10, again with different colors and line styles corresponding to different strain rates and microstructure IDs, respectively. The stress-strain curves are near-identical for all microstructure IDs within each strain rate, seen in the tight clustering of colors. As these microstructures were selected for having macroscopic responses closest to previous bulk experiments [26], they are expected to have near-identical macroscopic responses for a given strain rate. Though the simulated stresses have the same shape and fall within the same range as those in experiment (Fig. 8, compared in Fig. 11), the simulated responses instead show a strong strain rate-dependence. This rate-dependence is identified in the blue-black-red ordering with increasing stress, corresponding to an increase in flow stress with increasing strain rate. This result is expected, given that each simulated microstructure was tested at all 3 strain rates but each experimental sample was only tested at a single strain rate, confounding the effects of microstructure and strain rate in the latter.

Figures 12A-D show the evolution of lattice strains along LD with macroscopic strain in the 4 F microstructures for the same fibers as experiment. Only the $10^{-3}\,\mathrm{s}^{-1}$ simulations are shown, as the 10^{-4} and $10^{-2}\,\mathrm{s}^{-1}$ simulations show the same behaviors scaled by the expected rate-dependence (similar to the macroscopic data in Fig. 10) and as such do not provide additional insights. For these microstructures, the 3 lattice strains showing consistent ordering at yield are instead ε_{111} (blue), then ε_{311} (orange), then ε_{200} (purple), rather than ε_{220} (red), then ε_{311} (orange), then ε_{200} (purple) observed in experiment. Though ε_{200} is consistently the last to yield, its post-yield magnitude is much more variable than in experiment. This is most apparent in the unusually low magnitude of ε_{200} for F3 (Fig.

12C) and unusually high magnitude for F2 (Fig. 12B), with the former also showing suppressed hardening not observed for other microstructures. Variability is observed for ε_{220} (red) across the different microstructures, in disagreement with the ε_{111} (blue) variability of experiment (Fig. 9). With regard to its magnitude relative to the other lattice strains, ε_{220} was the smallest for F1 and F3 (Figs. 12A,C), fell between ε_{111} and ε_{311} for F2 (Fig. 12B), and crossed over ε_{111} for F4 (Fig. 12D). Here, ε_{220} generally follows the hardening behavior of the other lattice strains, but does show subtle softening right after yield in some cases, most apparent for F3 (Fig. 12C). These unusual behaviors were again independent of strain rate, as the same behaviors were observed at all 3 applied strain rates tested.

The macroscopic stress-strain responses of the 4 P microstructures tested at the 3 experimental strain rates are shown in Fig. 13 using the same color and line style scheme as the F microstructures. Unlike the F microstructures, the P microstructures show appreciable scatter within each strain rate (with different strain rates almost overlapping) despite being extracted from adjacent regions of the same larger voxelized microstructure. Note that, at large strains, these curves fall approximately 100 MPa below the experimental (Fig. 8) and F microstructure (Fig. 10) stress-strain curves. This is most apparent in Fig. 11 comparing the average macroscopic responses of the virtual microstructure sets and experiment at $10^{-3}\,\mathrm{s}^{-1}$. This difference in flow stress is a consequence of the same micromechanical parameters being used for all sets of simulated microstructures. These parameters were calibrated such that the macroscopic responses of the microstructures generated using the initial full ExaAM workflow (such as the F microstructures) would match experiment. The textures of those initial microstructures, however, were a poor match to the experimental textures, resulting in the macroscopic stress-strain curves deviating more from experiment when the calibrated parameters are applied to microstructures with textures better matching experiment.

Figures 14A-D show the evolution of lattice strains along LD with macroscopic strain in the 4 P microstructures for the same fibers as experiment. Again, only the $10^{-3}\,\mathrm{s}^{-1}$ simulations are shown. For these microstructures, the 3 lattice strains showing consistent ordering at yield are ε_{220} (red), then ε_{311} (orange), then ε_{200} (purple), matching what was observed in experiment (Fig. 9). Variability in ε_{111} is observed, although less extreme than that observed in experiment. ε_{111} falls below ε_{220} for P1 (Fig. 14A), falls on ε_{220} for P2 (Fig. 14B), and falls between ε_{220} and ε_{311} for P3 and P4 (Figs. 14C,D). For some

microstructures, ε_{111} appears to harden slightly faster (P2, P4) or slower (P1) than the other lattice strains. Unlike experiment or the F microstructures, the P microstructures show notable variability in the post-yield magnitude of ε_{311}. Justifications for the contrasts in the observed behaviors are discussed below.

4. Discussion

As seen in the results presented above, the micromechanical response of AM metals can vary drastically for the same homogenized macroscopic response, even for specimens sourced from adjacent sections of the same build. An understanding of the factors responsible would help inform simulation capabilities and accelerate AM process certification. To this end, a series of *in situ* high-energy X-ray diffraction experiments were performed at the FAST beamline at CHESS on AM IN625 under uniaxial compression. Micromechanical responses, quantified by average lattice strains along the loading direction for subsets of grains belonging to several crystallographic fibers, were extracted from the measured diffraction data and their evolution tracked as a function of macroscopic strain state. These findings were contextualized using *ex situ* measurements of orientation distribution. To help interpret these results, complementary CPFEM simulations were performed in ExaConstit on virtual microstructures generated in ExaCA. Rather than micromechanical response being solely influenced by directional strength-to-stiffness ratios, these findings, as will be shown below, point to the modulation of micromechanical response by grain neighborhood effects prompted by texture and morphology.

4.1. Role of Texture and Morphology

The stress-strain curves in Fig. 8 showed a lack of strain rate-dependence in the macroscopic response of the 6 experimental specimens, suggesting that the collective response is being dominated by variations in microtexture and morphology. If the experimentally probed diffraction volumes were larger than a representative volume element, then the macroscopic responses would instead be expected to group by strain rate, with faster strain rates corresponding to larger flow stresses [47, 48]. This microstructural dominance of macroscopic flow stress is not entirely surprising, as specimens are not expected to have statistically equivalent microstructures. This is because the specimens were extracted from the same vertical position in L7 (Fig. 1) but different locations throughout its cross-section and thus

different proximities to the leg edges, where a cube texture is known to exist [20]. In other words, strain rate effects are being overwhelmed by microstructural effects.

The effects of microstructure are most evident in the high variability of the {111} lattice strains (ε_{111}) in Fig. 9. The absence of measured {111} intensity along LD for all experimental samples compared to other lattice planes (Fig. 3) indicates that low volume fractions of grains belong to the fiber orienting ⟨111⟩ along BD/LD. In the context of the ⟨110⟩ and ⟨100⟩ fiber texture components observed for all samples, this points to the deformation of the subset of grains in the low-volume fraction ⟨111⟩ fiber being strongly constrained by the deformations of neighboring grains in the higher-volume fraction ⟨110⟩ and ⟨100⟩ fibers. ExaConstit simulations on virtual microstructures from ExaCA were used to further probe this proposed microstructure-dominated micromechanical response.

Comparing the experimental lattice strains to the virtual microstructures generated using the full ExaAM workflow (F), the lattice strains showing variability differ. The F microstructure lattice strains instead have consistent ε_{111} with variable ε_{220} (Fig. 12), though the variability of ε_{220} is less extreme than that observed for ε_{111} in experiment. There is also notable variability in the post-yield magnitude of ε_{200} despite its consistent yield order, demonstrated by F2 (Fig. 12B) and F3 (Fig. 12C), with F3 also uniquely showing suppressed hardening of this lattice strain. It was proposed above that the experimental ε_{111} variability was a consequence of neighborhood effects arising from the samples having ⟨110⟩ and ⟨100⟩ fiber texture components with an absence of {111} intensity along LD (Fig. 3). The orientation distributions for the F microstructures (e.g., Fig. 7A) instead show a ⟨111⟩ fiber texture component along LD/BD with low {220} and {200} intensity, the reverse of experiment. Since these virtual microstructures are fully described in 3D, it is apparent that the high-volume fraction ⟨111⟩ fiber primarily corresponds to the large columnar grains (Fig. 6A), while the low-volume fraction ⟨110⟩ and ⟨100⟩ fibers primarily correspond to the smaller grains between them. The disagreement in lattice strains displaying unusual behavior can be attributed to the swap in the orientation distributions along BD/LD for the corresponding crystallographic fibers, which corresponds to the predominant orientations of the large columnar grains. For the F microstructures, then, it would instead be the deformations of grains in the low-volume fraction ⟨110⟩ and ⟨100⟩ fibers being constrained by the deformations of grains in the high-volume fraction ⟨111⟩ fiber. This is consistent with the grain neighborhood effects proposed above.

Motivated by the results from the F microstructures, the P microstructures were instead generated using a phenomenological description of melt pool shapes and thermal histories in ExaCA in an effort to produce microstructures with textures more closely matching experiment. The orientation distributions for these microstructures (e.g., Fig. 7B) show that these microstructures exhibit ⟨110⟩ and ⟨100⟩ fiber texture components along BD, an absence of {111} density along BD, and somewhat uniform {311} density. By using a phenomenological description, the ⟨111⟩ fiber texture component characteristic of the F microstructures (Fig. 7A) was successfully suppressed. Looking at the P microstructures in 3D (e.g., Fig. 6B), large volume fractions of grains have ⟨110⟩ or ⟨100⟩ plane normals oriented along BD, with the large columnar grains preferring ⟨110⟩ and the smaller grains between them preferring ⟨100⟩. The P lattice strains (Fig. 14) are much closer to those for experiment (Fig. 9). The yield and post-yield behaviors of ε_{220} and ε_{200} are largely consistent across the microstructures, and the ε_{111} variability characteristic of experiment is present, though comparatively subdued. This variability occurs even for adjacent regions of the same larger microstructure (P1-4) with near-identical orientation distributions. This again points to the deformation of the subset of grains in the low-volume fraction ⟨111⟩ fiber being strongly constrained by the deformations of neighboring grains in the higher-volume fraction ⟨110⟩ and ⟨100⟩ fibers. The experimental behaviors being comparatively more extreme may be attributed to spatial variations in microstructure, as (1) the P microstructures collectively have the same dimensions as only one specimen scan volume ($1.0 \times 1.0 \times 0.5\,\text{mm}$) and (2) the specimen microstructures simulate only the center of L7, whereas the experimental specimens were extracted from throughout the leg cross-section. The ε_{311} variability observed for the P microstructures (but not experiment) may be attributed to the somewhat lower {311} density along BD for all microstructures (e.g., Fig. 7B) in the same manner as for ε_{111}. It is interesting, however, that this behavior was not observed in the experimental lattice strains (Fig. 9), for which the lower {311} density along BD was also observed (Fig. 3).

4.2. Role of Directional Strength-to-Stiffness Ratios

Wong and Dawson showed that directional strength-to-stiffness ratios (Eq. 12) are good indicators of the order in which subsets of grains belonging to different crystallographic fibers yield, with grains in fibers having higher ratios yielding on average at a higher macroscopic stress and vice versa [46]. They concluded, however, that this held only for crystals

with extremely low or high single-crystal elastic anisotropy, observing that grain neighborhood effects weaken the influence of these ratios for materials with moderate single-crystal elastic anisotropy. In other words, grain neighborhood effects become as significant as directional strength-to-stiffness in the latter case. Wong and Dawson quantified elastic anisotropy with the directional stiffness ratio E_{111}/E_{100}, where E_{111} and E_{100} are the single-crystal elastic moduli along the respective crystallographic directions. They defined extremes of 1 (isotropic) and 3 (highly anisotropic), with $1.4 - 1.6$ constituting moderate elastic anisotropy [46]. Note that this defined ratio differs from the standard cubic Zener ratio, which is 2.72 for this material. This directional stiffness ratio was 2.42 for the virtual IN625 microstructures studied in this work, indicating high elastic anisotropy. The directional strength-to-stiffness ratios, then, would be expected to dominate the yield order and grain neighborhood effects would not be expected to cause deviations from this order. With grain neighborhood effects, rather than directional strength-to-stiffness, posited as the explanation for the micromechanical behaviors observed across experiment and simulation in this work, these ratios were calculated for the simulated microstructures to assess their role.

Figure 15 shows the calculated fiber-averaged strength-to-stiffness ratios for all simulated microstructures in this work, with the ratios for the F and P microstructures shown in Figs. 15A and 15B, respectively. These ratios are relatively consistent across most microstructures in both order and approximate value despite the differences in texture between them, with $r_{200} > r_{311} > r_{111} > r_{220}$. This indeed corresponds to the yield order (ε_{220} (red), then ε_{111} (blue), then ε_{311} (orange), then ε_{200} (purple)) for most of the simulated microstructures, consistent with grains in crystallographic fibers with higher directional strength-to-stiffness ratios yielding on average after grains in fibers with lower ratios. The exceptions to the ratio orders are F4, for which $r_{111} \approx r_{220}$, and P4, for which $r_{111} \approx r_{311}$. However, these microstructures have the common yield order indicated above, inconsistent with their atypical strength-to-stiffness ratio orders. Moreover, the microstructures with atypical lattice strain yield orders and other behaviors described above do not correspond to any unusual strength-to-stiffness ratios. We emphasize that different virtual microstructures have different fiber yield orders despite most having the same strength-to-stiffness ratio order, and atypical behaviors in one quantity do not correlate to atypical behaviors in the other. As a material with high elastic anisotropy, this behavior is unexpected under the findings of

Wong and Dawson. However, their investigation of polycrystals considered only rhombic dodecahedral (i.e., pseudo-equiaxed) grains with orientations randomly sampled from a uniform orientation distribution. Such an instantiation is not representative of the textured, columnar AM microstructures considered in this work (Figs. 6 and 7). Furthermore, Figs. 2 and 6B highlight that these microstructures also have specific *grain configurations*, having tracks of fine $\langle 100 \rangle$-oriented grains along x between the large, columnar $\langle 110 \rangle$-oriented grains. We therefore assert that the textures and morphologies (and configurations) of these AM microstructures result in grain neighborhood effects on micromechanical response sufficient to overwhelm directional strength-to-stiffness even in cases of high elastic anisotropy. These findings point to the importance of high-fidelity microstructural representation in predicting the micromechanical response of AM metals.

5. Conclusions

In this work, *in situ* high-energy X-ray diffraction experiments were used to simultaneously collect macro- and micromechanical data for AM IN625 under uniaxial compression. Complementary cellular automata and crystal plasticity finite element method simulations were then used to help interpret experimental findings to probe the effects of texture and grain morphology on the micromechanical response of AM IN625, supporting micromechanical model development for AM materials and certification of AM processes. The key findings are summarized below:

- Variation in texture and microtexture produced modest variation in flow stress that was sufficient to overwhelm the effects of strain rate-dependence. For both experiment and simulation, specimens with comparable macroscopic responses displayed distinctly different mesoscopic deformation states.
- Texture and columnar grain morphology strongly modulated micromechanical response. The experimental samples and full workflow virtual microstructures displayed variability and unique hardening and softening behaviors for different lattice strains along the loading direction, directly corresponding to different volume fractions and configurations of grain orientations. The phenomenological virtual microstructures had textures most closely resembling experiment and best captured the micromechanical characteristics of experiment.

- Across the simulated microstructures, the orders in which different subsets of grain orientations yielded were not fully consistent with their corresponding directional strength-to-stiffness ratios despite the high single-crystal elastic anisotropy of IN625. The deviations are proposed to be due to neighborhood interactions among grains, driven by the textures and columnar grain morphologies characteristic of these AM microstructures, overwhelming directional strength-to-stiffness.

Together, the above observations across experiment and simulation indicate that grain neighborhood effects strongly modulate micromechanical response for these AM metals. These findings informed development of ExaCA and ExaConstit in demonstrating the importance of incorporating realistic microstructures for accurate prediction of micromechanical response.

6. Acknowledgments

We thank Dr. Lyle Levine (NIST) for providing the bridge specimen from which the compression specimens were extracted. We also thank Dr. Alyssa Maich (LLNL) for collecting the EBSD data presented in Section 2. RJK and DCP acknowledge support from LLNL Contract #B652591. This work is based on research conducted at the Center for High-Energy X-ray Sciences (CHEXS) at CHESS, which is supported by the National Science Foundation (BIO, ENG, and MPS Directorates) under award DMR-1829070. This research was supported by the Exascale Computing Project (17-SC-20-SC), a collaborative effort of the U.S. DOE Office of Science and the NNSA. This work was performed under the auspices of the U.S. Department of Energy by Lawrence Livermore National Laboratory under Contract DE-AC52-07NA27344. This manuscript has been in part authored by UT-Battelle, LLC, under contract DE-AC05-00OR22725 with the U.S. Department of Energy (DOE).

7. Data Availability

All data used for this work are available upon reasonable request.

References

[1] M. Sangid, S. Yeratapally, A. Rovinelli, Validation of microstructure-based materials modeling, in: 55th AIAA/ASMe/ASCE/AHS/SC Structures, Structural Dynamics, and Materials Conference, 2014, p. 0462. doi:10.2514/6.2014-0462.

[2] R. Bandyopadhyay, P. Veerappan, M. Sangid, Uncertainty quantification in the mechanical response of crystal plasticity simulations, JOM 71 (06 2019). doi:10.1007/s11837-019-03551-3.

[3] R. Bandyopadhyay, S. E. Gustafson, K. Kapoor, D. Naragani, D. C. Pagan, M. D. Sangid, Comparative assessment of backstress models using high-energy X-ray diffraction microscopy experiments and crystal plasticity finite element simulations, International Journal of Plasticity 136 (2021) 102887. doi:https://doi.org/10.1016/j.ijplas.2020.102887.
URL https://www.sciencedirect.com/science/article/pii/S0749641920302370

[4] B. T. Mackey, R. Bandyopadhyay, S. E. Gustafson, M. D. Sangid, Grain interactions under thermo-mechanical loads investigated with coupled crystal plasticity simulations and high-energy X-ray diffraction microscopy, Acta Materialia 257 (2023) 119166. doi:https://doi.org/10.1016/j.actamat.2023.119166.
URL https://www.sciencedirect.com/science/article/pii/S1359645423004974

[5] R. Quey, P. Dawson, J. Driver, Grain orientation fragmentation in hot-deformed aluminium: Experiment and simulation, Journal of the Mechanics and Physics of Solids 60 (3) (2012) 509–524. doi:https://doi.org/10.1016/j.jmps.2011.11.005.
URL https://www.sciencedirect.com/science/article/pii/S0022509611002171

[6] P. Dawson, D. Boyce, S. MacEwen, R. Rogge, Residual strains in HY100 polycrystals: Comparisons of experiments and simulations, Metallurgical and Materials Transactions A 31 (6) (2000) 1543–1555. doi:10.1007/s11661-000-0165-4.
URL http://dx.doi.org/10.1007/s11661-000-0165-4

[7] C. Efstathiou, D. Boyce, J.-S. Park, U. Lienert, P. Dawson, M. Miller, A method for measuring single-crystal elastic moduli using high-energy X-ray diffraction and a crystal-based finite element model, Acta Materialia 58 (17) (2010) 5806–5819.

doi:https://doi.org/10.1016/j.actamat.2010.06.056.
URL https://www.sciencedirect.com/science/article/pii/S1359645410004210

[8] E. Wielewski, D. E. Boyce, J.-S. Park, M. P. Miller, P. R. Dawson, A methodology to determine the elastic moduli of crystals by matching experimental and simulated lattice strain pole figures using discrete harmonics, Acta Materialia 126 (2017) 469–480. doi:https://doi.org/10.1016/j.actamat.2016.12.026.
URL https://www.sciencedirect.com/science/article/pii/S1359645416309624

[9] D. C. Pagan, P. A. Shade, N. R. Barton, J.-S. Park, P. Kenesei, D. B. Menasche, J. V. Bernier, Modeling slip system strength evolution in Ti-7Al informed by in-situ grain stress measurements, Acta Materialia 128 (2017) 406–417. doi:https://doi.org/10.1016/j.actamat.2017.02.042.
URL https://www.sciencedirect.com/science/article/pii/S1359645417301337

[10] S. L. Wong, M. Obstalecki, M. P. Miller, P. R. Dawson, Stress and deformation heterogeneity in individual grains within polycrystals subjected to fully reversed cyclic loading, Journal of the Mechanics and Physics of Solids 79 (2015) 157–185. doi:https://doi.org/10.1016/j.jmps.2015.03.010.
URL https://www.sciencedirect.com/science/article/pii/S0022509615000666

[11] R. Carson, M. Obstalecki, M. Miller, P. Dawson, Characterizing heterogeneous intragranular deformations in polycrystalline solids using diffraction-based and mechanics-based metrics, Modelling and Simulation in Materials Science and Engineering 25 (5) (2017) 055008. doi:10.1088/1361-651X/aa6dc5.
URL https://dx.doi.org/10.1088/1361-651X/aa6dc5

[12] L. E. Murr, E. Martinez, S. M. Gaytan, D. A. Ramirez, B. I. Machado, P. W. Shindo, J. L. Martinez, F. Medina, J. Wooten, D. Ciscel, U. Ackelid, R. B. Wicker, Microstructural architecture, microstructures, and mechanical properties for a nickel-base superalloy fabricated by electron beam melting, Metallurgical and Materials Transactions A 42 (11) (2011) 3491–3508. doi:10.1007/s11661-011-0748-2.
URL http://dx.doi.org/10.1007/s11661-011-0748-2

[13] D. Zhang, D. Qiu, M. A. Gibson, Y. Zheng, H. L. Fraser, D. H. StJohn, M. A. Easton, Additive manufacturing of ultrafine-grained high-strength titanium alloys, Nature

576 (7785) (2019) 91–95. doi:10.1038/s41586-019-1783-1.
URL http://dx.doi.org/10.1038/s41586-019-1783-1

[14] Y. Zhu, K. Zhang, Z. Meng, K. Zhang, P. Hodgson, N. Birbilis, M. Weyland, H. L. Fraser, S. C. V. Lim, H. Peng, R. Yang, H. Wang, A. Huang, Ultrastrong nanotwinned titanium alloys through additive manufacturing, Nature Materials 21 (11) (2022) 1258–1262. doi:10.1038/s41563-022-01359-2.
URL http://dx.doi.org/10.1038/s41563-022-01359-2

[15] W. A. Witzen, A. T. Polonsky, T. M. Pollock, I. J. Beyerlein, Three-dimensional maps of geometrically necessary dislocation densities in additively manufactured Ni-based superalloy IN718, International Journal of Plasticity 131 (2020) 102709. doi:https://doi.org/10.1016/j.ijplas.2020.102709.
URL https://www.sciencedirect.com/science/article/pii/S0749641919306473

[16] L. Levine, B. Lane, J. Heigel, K. Migler, M. Stoudt, T. Phan, R. Ricker, M. Strantza, M. Hill, F. Zhang, J. Seppala, E. Garboczi, E. Bain, D. Cole, A. Allen, J. Fox, C. Campbell, Outcomes and conclusions from the 2018 AM-Bench measurements, challenge problems, modeling submissions, and conference, Integrating Materials and Manufacturing Innovation 9 (1) (2020) 1–15. doi:10.1007/s40192-019-00164-1.
URL http://dx.doi.org/10.1007/s40192-019-00164-1

[17] L. E. Levine, B. Lane, AMB2018-01 description, https://www.nist.gov/ambench/amb2018-01-description (Jul. 2023).
URL https://www.nist.gov/ambench/amb2018-01-description

[18] L. E. Levine, B. Lane, CHAL-AMB2018-01-MSPFPFRS, https://www.nist.gov/ambench/chal-amb2018-01-mspfpfrs (Jul. 2023).
URL https://www.nist.gov/ambench/chal-amb2018-01-mspfpfrs

[19] M. H. Şeren, D. C. Pagan, I. C. Noyan, Representative volume elements of strain/stress fields measured by diffraction techniques, Journal of Applied Crystallography 56 (4) (2023) 1144–1167. doi:https://doi.org/10.1107/S1600576723004351.

[20] L. Levine, D. Rowenhorst, A. Maich, A. Creuziger, R. Carson, N. Raghavan, AM Bench 2022 microstructure measurement follow-on for AM Bench 2018 IN625 3d builds (2023).

doi:10.18434/MDS2-2712.
URL https://data.nist.gov/od/id/mds2-2712

[21] P. A. Shade, B. Blank, J. C. Schuren, T. J. Turner, P. Kenesei, K. Goetze, R. M. Suter, J. V. Bernier, S. F. Li, J. Lind, U. Lienert, J. Almer, A rotational and axial motion system load frame insert for in situ high energy x-ray studies, Review of Scientific Instruments 86 (9) (2015) 093902. arXiv:https://pubs.aip.org/aip/rsi/article-pdf/doi/10.1063/1.4927855/15830098/093902_1_online.pdf, doi:10.1063/1.4927855.
URL https://doi.org/10.1063/1.4927855

[22] S. R. Kalidindi, A. Abusafieh, E. El-Danaf, Accurate characterization of machine compliance for simple compression testing, Experimental Mechanics 37 (2) (1997) 210–215. doi:10.1007/bf02317861.
URL http://dx.doi.org/10.1007/bf02317861

[23] F. Bachmann, R. Hielscher, H. Schaeben, Texture analysis with MTEX – free and open source software toolbox, in: Texture and Anisotropy of Polycrystals III, Vol. 160 of Solid State Phenomena, Trans Tech Publications Ltd, 2010, pp. 63–68. doi:10.4028/www.scientific.net/SSP.160.63.

[24] Z. Wang, A. D. Stoica, D. Ma, A. M. Beese, Diffraction and single-crystal elastic constants of Inconel 625 at room and elevated temperatures determined by neutron diffraction, Materials Science and Engineering: A 674 (2016) 406–412. doi:https://doi.org/10.1016/j.msea.2016.08.010.
URL https://www.sciencedirect.com/science/article/pii/S0921509316309133

[25] M. Rolchigo, R. Carson, J. Belak, Understanding uncertainty in microstructure evolution and constitutive properties in additive process modeling, Metals 12 (2) (2022). doi:10.3390/met12020324.
URL https://www.mdpi.com/2075-4701/12/2/324

[26] R. Carson, M. Rolchigo, J. Coleman, M. Titov, J. Belak, M. Bement, Uncertainty quantification of metal additive manufacturing processing conditions through the use of exascale computing, in: Proceedings of the SC '23 Workshops of The International Conference on High Performance Computing, Network, Storage, and Analysis, SC-W '23, Association for Computing Machinery, New York, NY, USA, 2023, p. 380–383.

doi:10.1145/3624062.3624103.
URL https://doi.org/10.1145/3624062.3624103

[27] S. Wells, A. Plotkowski, J. Coleman, M. Rolchigo, R. Carson, M. Krane, Uncertainty quantification for computational modelling of laser powder bed fusion, in: IOP Conference Series: Materials Science and Engineering, Vol. 1281, IOP Publishing, 2023, p. 012024.

[28] M. Rolchigo, S. Reeve, J. Stump, C. Junghans, LLNL/ExaCA: Version 1.2 (May 2023). doi:10.5281/zenodo.7931062.
URL https://doi.org/10.5281/zenodo.7931062

[29] M. Rolchigo, J. Coleman, G. L. Knapp, A. Plotkowski, Grain structure and texture selection regimes in metal powder bed fusion, Additive Manufacturing 81 (2024) 104024. doi:https://doi.org/10.1016/j.addma.2024.104024.
URL https://www.sciencedirect.com/science/article/pii/S2214860424000708

[30] M. Rolchigo, S. T. Reeve, B. Stump, G. L. Knapp, J. Coleman, A. Plotkowski, J. Belak, ExaCA: A performance portable exascale cellular automata application for alloy solidification modeling, Computational Materials Science 214 (2022) 111692. doi:https://doi.org/10.1016/j.commatsci.2022.111692.
URL https://www.sciencedirect.com/science/article/pii/S0927025622004189

[31] C.-A. Gandin, M. Rappaz, A 3d cellular automaton algorithm for the prediction of dendritic grain growth, Acta Materialia 45 (5) (1997) 2187–2195. doi:https://doi.org/10.1016/S1359-6454(96)00303-5.
URL https://www.sciencedirect.com/science/article/pii/S1359645496003035

[32] M. Titov, R. Carson, M. Rolchigo, J. Coleman, J. Belak, M. Bement, D. Laney, M. Turilli, S. Jha, Scaling on frontier: Uncertainty quantification workflow applications using exaworks to enable full system utilization, arXiv preprint arXiv:2407.01484 (2024).

[33] J. Coleman, K. Kincaid, G. L. Knapp, B. Stump, A. J. Plotkowski, AdditiveFOAM: Release 1.0 (Jun. 2023). doi:10.5281/zenodo.8034098.
URL https://doi.org/10.5281/zenodo.8034098

[34] R. A. Carson, S. R. Wopschall, J. A. Bramwell, ExaConstit, [Computer Software] https://doi.org/10.11578/dc.20191024.2 (Aug. 2019). doi:10.11578/dc.20191024.2.
URL https://github.com/LLNL/ExaConstit

[35] J. A. Turner, J. Belak, N. Barton, M. Bement, N. Carlson, R. Carson, S. DeWitt, J.-L. Fattebert, N. Hodge, Z. Jibben, W. King, L. Levine, C. Newman, A. Plotkowski, B. Radhakrishnan, S. T. Reeve, M. Rolchigo, A. Sabau, S. Slattery, B. Stump, ExaAM: Metal additive manufacturing simulation at the fidelity of the microstructure, The International Journal of High Performance Computing Applications 36 (1) (2022) 13–39. arXiv:https://doi.org/10.1177/10943420211042558, doi:10.1177/10943420211042558.
URL https://doi.org/10.1177/10943420211042558

[36] N. R. Barton, R. A. Carson, S. R. Wopschall, U. N. N. S. Administration, ECMech (12 2018). doi:10.11578/dc.20190809.2.
URL https://github.com/LLNL/ExaCMech

[37] E. Marin, P. Dawson, On modelling the elasto-viscoplastic response of metals using polycrystal plasticity, Computer Methods in Applied Mechanics and Engineering 165 (1) (1998) 1–21. doi:https://doi.org/10.1016/S0045-7825(98)00034-6.
URL https://www.sciencedirect.com/science/article/pii/S0045782598000346

[38] R. Anderson, J. Andrej, A. Barker, J. Bramwell, J.-S. Camier, J. Cerveny, V. Dobrev, Y. Dudouit, A. Fisher, T. Kolev, W. Pazner, M. Stowell, V. Tomov, I. Akkerman, J. Dahm, D. Medina, S. Zampini, MFEM: A Modular Finite Element Methods Library, Computers & Mathematics with Applications 81 (2021) 42–74. doi:10.1016/j.camwa.2020.06.009.

[39] B. E. Carroll, R. A. Otis, J. P. Borgonia, J. ook Suh, R. P. Dillon, A. A. Shapiro, D. C. Hofmann, Z.-K. Liu, A. M. Beese, Functionally graded material of 304L stainless steel and Inconel 625 fabricated by directed energy deposition: Characterization and thermodynamic modeling, Acta Materialia 108 (2016) 46–54. doi:https://doi.org/10.1016/j.actamat.2016.02.019.
URL https://www.sciencedirect.com/science/article/pii/S1359645416300908

[40] Z. Wang, E. Denlinger, P. Michaleris, A. D. Stoica, D. Ma, A. M. Beese, Residual stress mapping in Inconel 625 fabricated through additive manufacturing: Method for neutron diffraction measurements to validate thermomechanical model predictions, Materials & Design 113 (2017) 169–177. doi:https://doi.org/10.1016/j.matdes.2016.10.003.
URL https://www.sciencedirect.com/science/article/pii/S0264127516312941

[41] A. M. Beese, Z. Wang, A. D. Stoica, D. Ma, Absence of dynamic strain aging in an additively manufactured nickel-base superalloy, Nature Communications 9 (1) (May 2018). doi:10.1038/s41467-018-04473-5.
URL http://dx.doi.org/10.1038/s41467-018-04473-5

[42] A. M. Beese, Chapter 5 - microstructure and mechanical properties of am builds, in: M. Gouge, P. Michaleris (Eds.), Thermo-Mechanical Modeling of Additive Manufacturing, Butterworth-Heinemann, 2018, pp. 81–92. doi:https://doi.org/10.1016/B978-0-12-811820-7.00007-0.
URL https://www.sciencedirect.com/science/article/pii/B9780128118207000070

[43] Z. Wang, A. D. Stoica, D. Ma, A. M. Beese, Stress relaxation in a nickel-base superalloy at elevated temperatures with in situ neutron diffraction characterization: Application to additive manufacturing, Materials Science and Engineering: A 714 (2018) 75–83. doi:https://doi.org/10.1016/j.msea.2017.12.058.
URL https://www.sciencedirect.com/science/article/pii/S0921509317316556

[44] S. Qin, T. C. Novak, M. K. Vailhe, Z.-K. Liu, A. M. Beese, Plasticity and fracture behavior of Inconel 625 manufactured by laser powder bed fusion: Comparison between as-built and stress relieved conditions, Materials Science and Engineering: A 806 (2021) 140808. doi:https://doi.org/10.1016/j.msea.2021.140808.
URL https://www.sciencedirect.com/science/article/pii/S0921509321000770

[45] J. Bernier, P. Avery, S. Soderlind, D. Boyce, B. Major, Z. Singer, K. Nygren, P. Shade, HEXRD/hexrd: Release 0.9.4, [Computer Software] https://doi.org/10.5281/zenodo.10028150 (Oct. 2023). doi:10.5281/zenodo.10028150.
URL https://doi.org/10.5281/zenodo.10028150

[46] S. Wong, P. Dawson, Influence of directional strength-to-stiffness on the elastic–plastic transition of fcc polycrystals under uniaxial tensile loading, Acta Materialia 58 (5) (2010) 1658–1678. doi:https://doi.org/10.1016/j.actamat.2009.11.009.
URL https://www.sciencedirect.com/science/article/pii/S1359645409007848

[47] U. F. Kocks, Laws for Work-Hardening and Low-Temperature Creep, Journal of Engineering Materials and Technology 98 (1) (1976) 76–85. arXiv:https://asmedigitalcollection.asme.org/materialstechnology/article-pdf/98/1/76/5593266/76_1.pdf, doi:10.1115/1.3443340.
URL https://doi.org/10.1115/1.3443340

[48] P. Follansbee, U. Kocks, A constitutive description of the deformation of copper based on the use of the mechanical threshold stress as an internal state variable, Acta Metallurgica 36 (1) (1988) 81–93. doi:https://doi.org/10.1016/0001-6160(88)90030-2.
URL https://www.sciencedirect.com/science/article/pii/0001616088900302

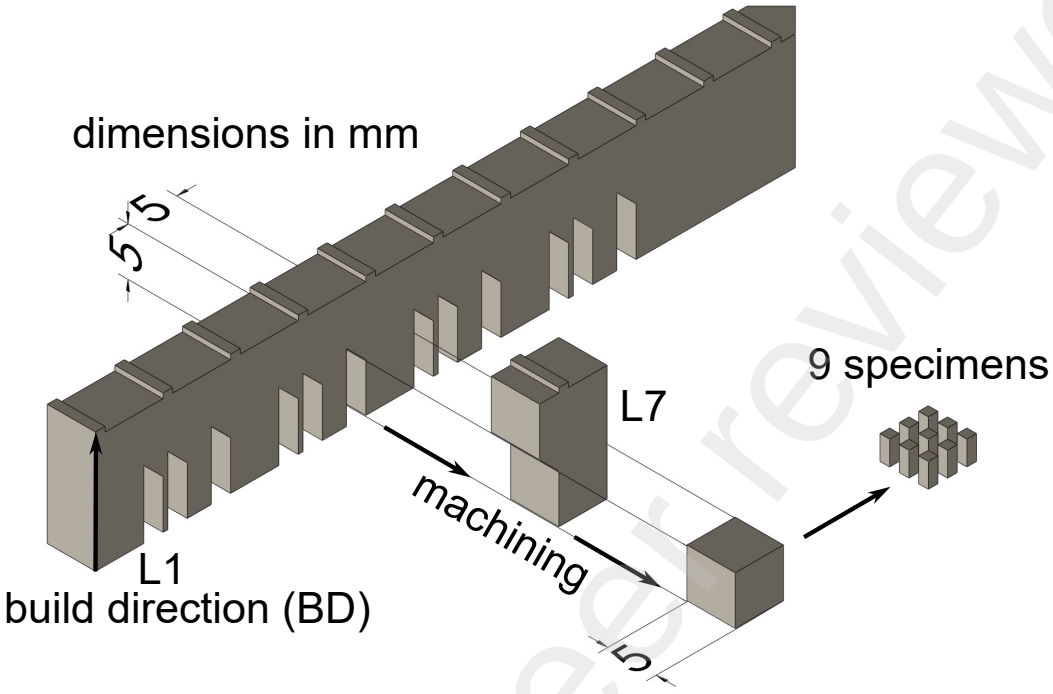

Figure 1: Schematic of an AMB2018-01 LPBF build. For these experiments, specimens were extracted from leg 7 (L7) as indicated. The build direction (BD) is marked. Modified from an STL file taken from [17].

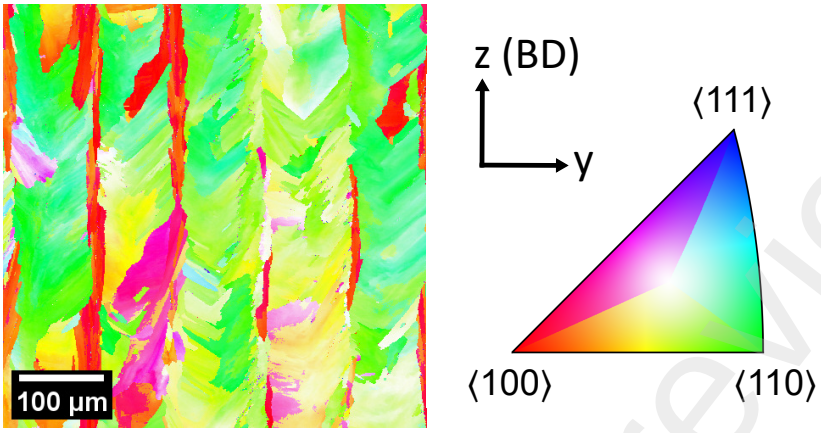

Figure 2: EBSD data for a 0.5×0.5 mm region from the interior of L1. Inverse pole figure coloring is with respect to the specimen build direction (BD).

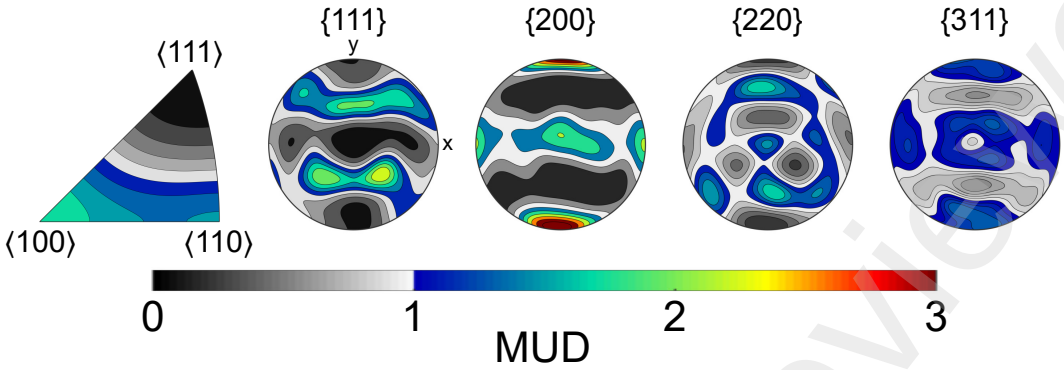

Figure 3: Orientation distribution represented with inverse pole figure of BD/LD (left) and pole figures (right, BD out-of-plane) in multiples of uniform density (MUD) for sample E1, representative of most experimental specimens.

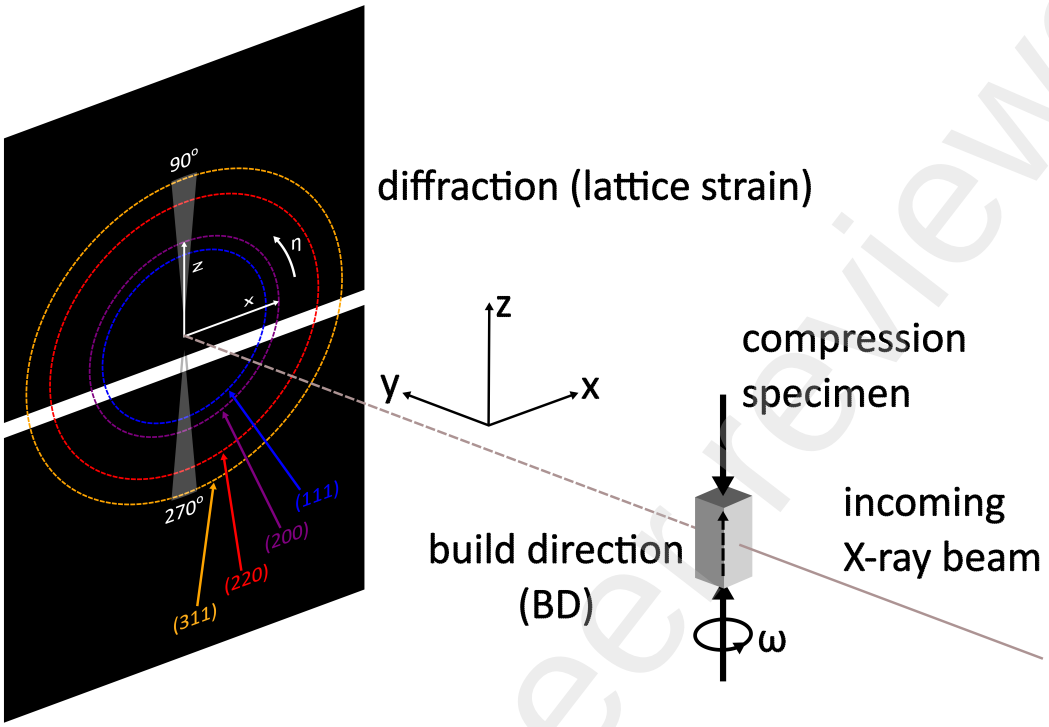

Figure 4: Schematic of the experimental geometry for X-ray data collection, showing the laboratory coordinate axes, azimuthal angle η, and specimen rotation angle ω. The first 4 Debye-Scherrer rings for IN625 are shown in their approximate positions on the vertically stacked detector arrangement.

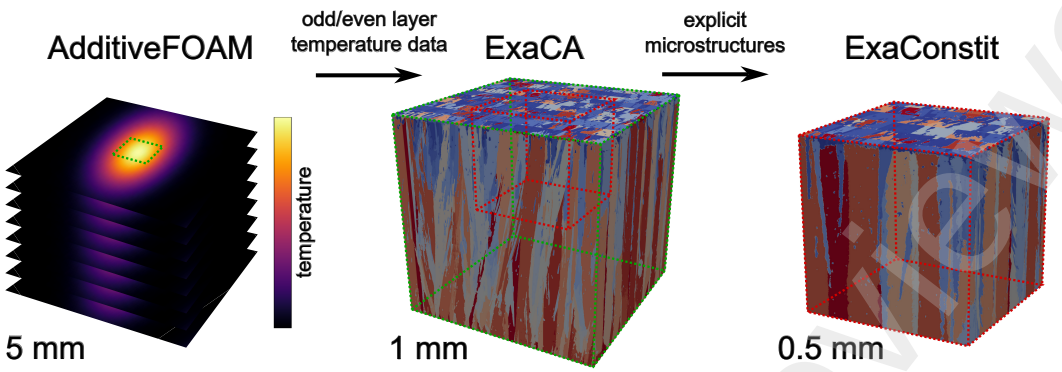

Figure 5: Schematic describing generation of explicit microstructures for ExaConstit simulations. Representative odd/even layer temperature data from AdditiveFOAM are used by ExaCA to generate explicit microstructures from which smaller volumes are extracted and meshed for use in ExaConstit.

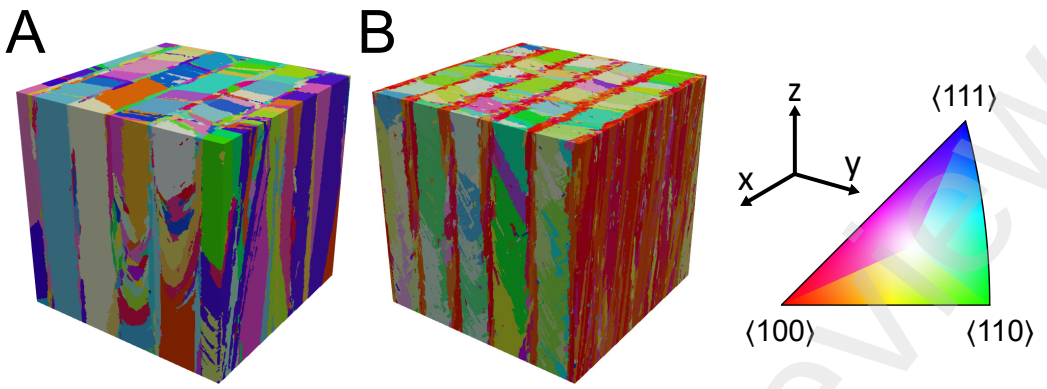

Figure 6: Simulated microstructures ($0.5 \times 0.5 \times 0.5\,\mathrm{mm}$) (A) F1 and (B) P1 with IPF-z coloring, each representative of their respective microstructure sets.

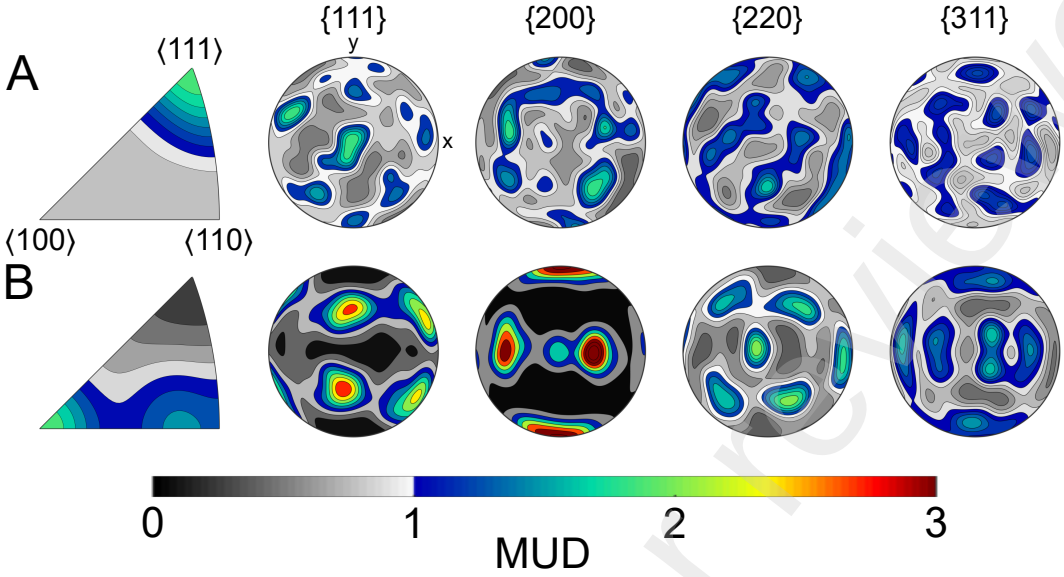

Figure 7: Orientation distributions represented with inverse pole figures of BD/LD (left) and pole figures (right, BD out-of-plane) for simulated microstructures (A) F1 and (B) P1, each representative of their respective microstructure sets.

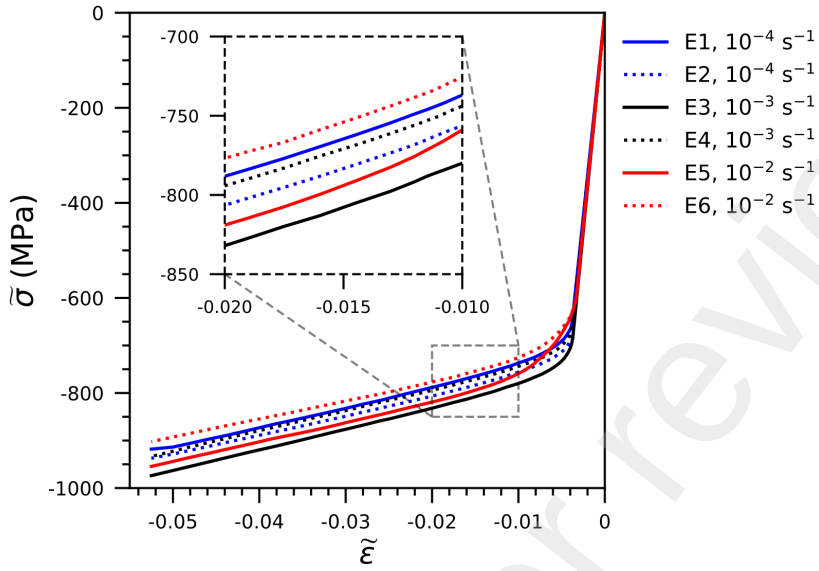

Figure 8: Macroscopic stress-strain curves for all experimental samples colored by strain rate, with different line styles used to indicate specimen ID for each strain rate.

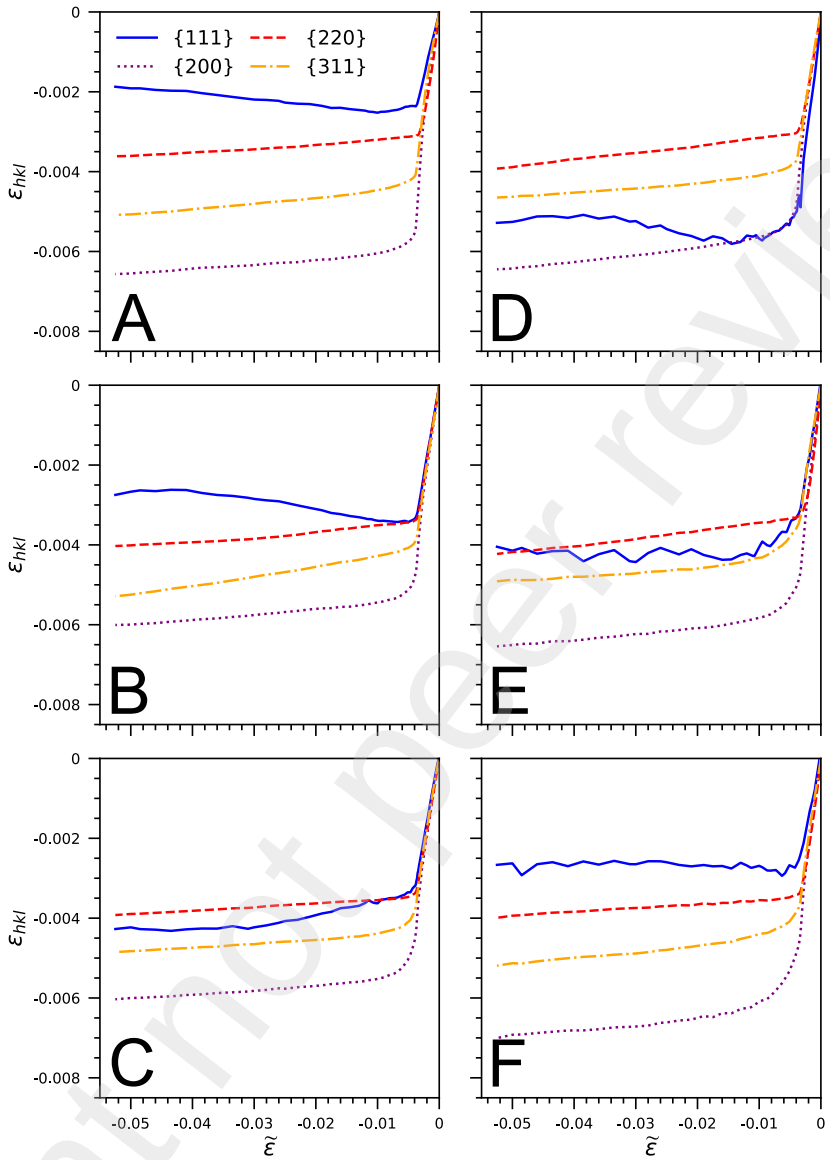

Figure 9: Experimental lattice strains as a function of macroscopic strain for samples (A-F) E1-E6.

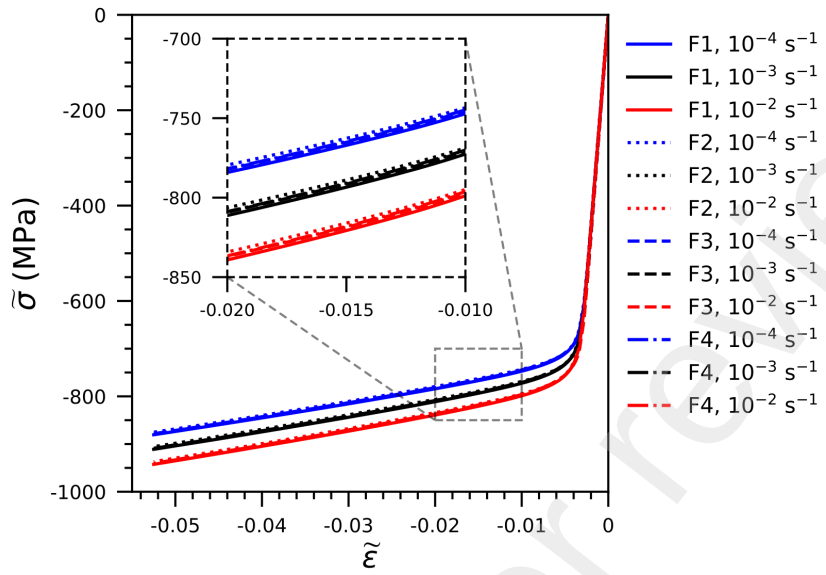

Figure 10: Macroscopic stress-strain curves for microstructures F1-4, each tested at 3 strain rates (10^{-4}, 10^{-3}, $10^{-2}\,s^{-1}$). Curves are colored by strain rate, with different line styles indicating microstructure ID.

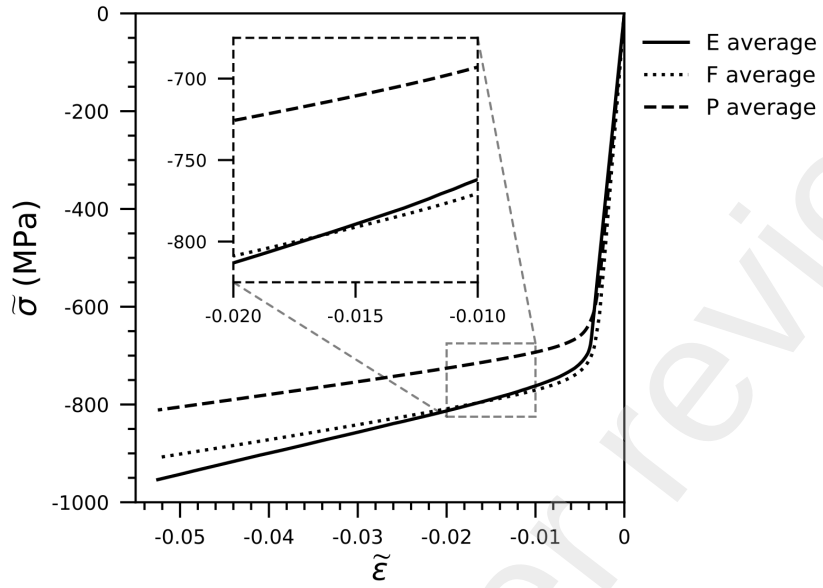

Figure 11: Average macroscopic stress-strain curves for the experimental data (E3 and E4) and the F and P microstructures at $10^{-3}\,\mathrm{s}^{-1}$. Different line styles indicate microstructure set.

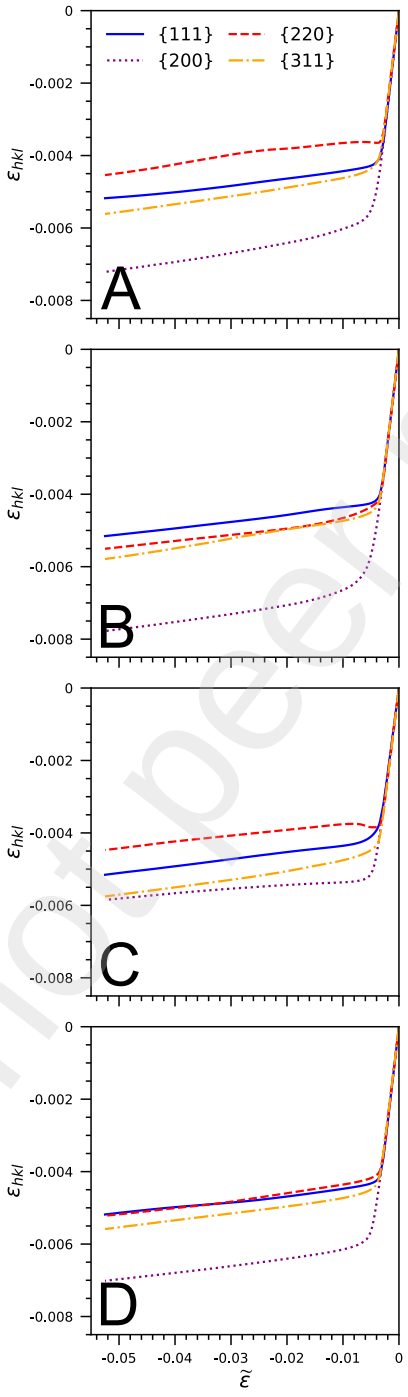

Figure 12: Lattice strains for microstructures (A-D) F1-4 at $10^{-3}\,\mathrm{s}^{-1}$ strain rate.

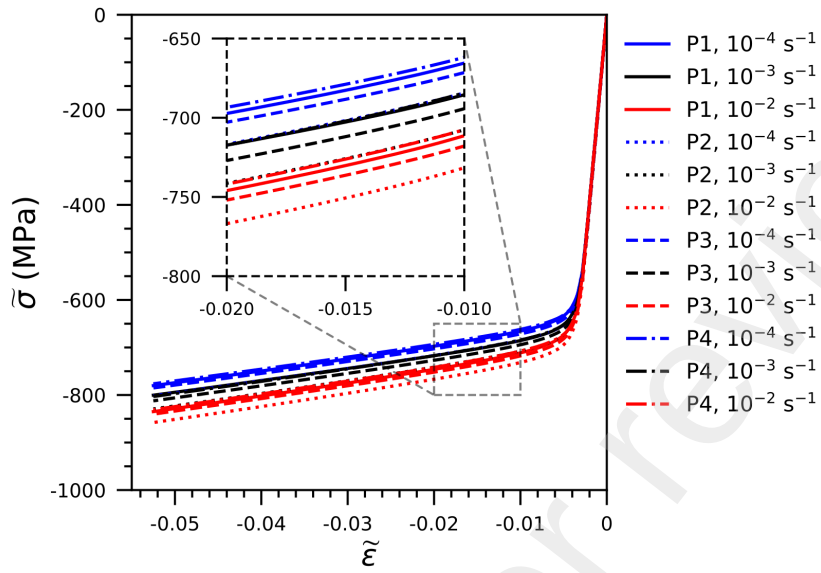

Figure 13: Macroscopic stress-strain curves for microstructures P1-4, each tested at 3 strain rates (10^{-4}, 10^{-3}, $10^{-2}\,s^{-1}$). Curves are colored by strain rate, with different line styles indicating microstructure ID.

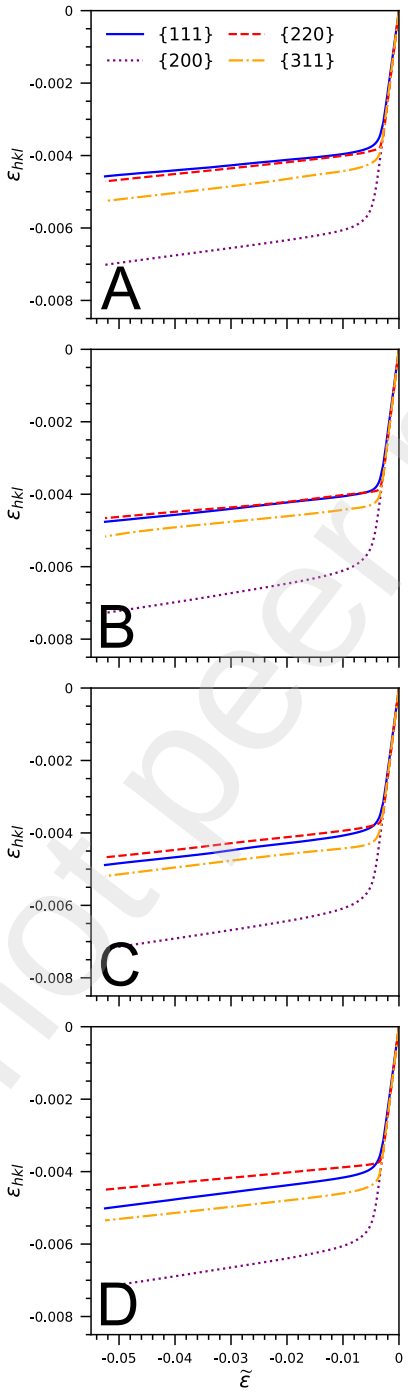

Figure 14: Lattice strains for microstructures (A-D) P1-4 at $10^{-3}\,\mathrm{s}^{-1}$ strain rate.

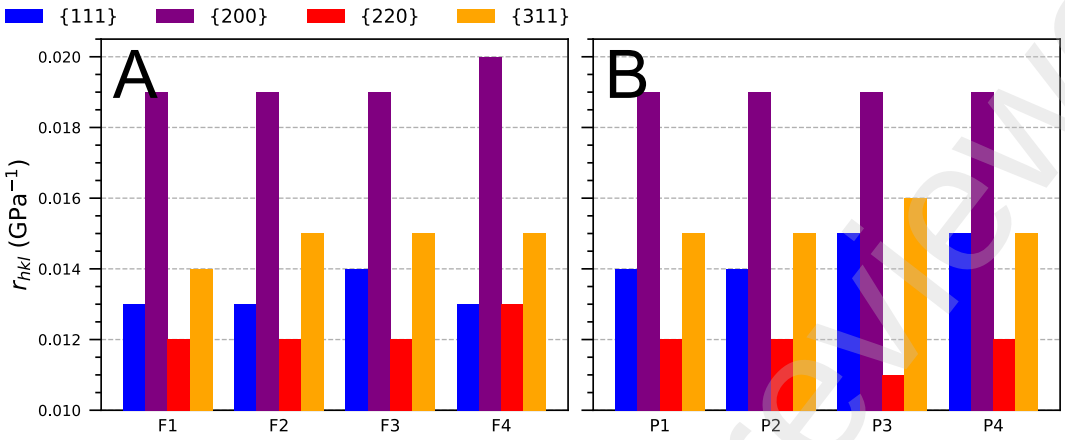

Figure 15: Directional strength-to-stiffness ratios for the 4 crystallographic fibers examined for the (A) F and (B) P microstructures.

Table 1: Summary of EOS M270 build parameters for NIST AMB2018-01 LPBF build [16, 17].

Build Parameter	Value
number of layers	625
layer height	20 µm
contour scan speed	900 mm/s
contour laser power	100 W
infill scan speed	800 mm/s
infill laser power	195 W
hatch distance	100 µm
time between infill scan lines	6.70 ms
laser spot size full-width-half-max	≈ 50 µm
inert gas	N_2
O_2 level	$\approx 0.5\%$

Table 2: Specimen/microstructure labeling scheme, including specimen/microstructure sets and the region of the $1 \times 1 \times 1$ mm ExaCA volume from which the $0.5 \times 0.5 \times 0.5$ mm virtual microstructures were taken for ExaConstit.

specimen/microstructure sets

Label	Origin	Count
E	real (experiment)	6
F	virtual (full ExaAM workflow)	4
P	virtual (phenomenological)	4

ExaCA bounds for virtual microstructures

Label	x Bounds (mm)	y Bounds (mm)	z Bounds (mm)
F1-4	$[0.25, 0.75]$	$[0.25, 0.75]$	$[0.5, 1]$
P1	$[0, 0.5]$	$[0, 0.5]$	$[0.5, 1]$
P2	$[0.5, 1]$	$[0, 0.5]$	$[0.5, 1]$
P3	$[0, 0.5]$	$[0.5, 1]$	$[0.5, 1]$
P4	$[0.5, 1]$	$[0.5, 1]$	$[0.5, 1]$

Table 3: Micromechanical parameters used for ExaConstit simulations. These parameters are inputs for anisotropic elasticity with power law slip and linear Voce hardening.

Parameter	Symbol	Value	Unit
	c_{11}	243.3	GPa
elastic constants	c_{12}	156.7	GPa
	c_{44}	117.8	GPa
rate exponent	m	0.015	-
base shearing rate	$\dot{\gamma}_0$	1.0	s^{-1}
hardening coefficient	h_0	485.0	MPa
initial CRSS	g_0	312.75	MPa
saturation CRSS	g_s	745.0	MPa

Appendix A. Experimental Orientation Distributions

Figure A.16 shows the IPFs and PFs for all experimental specimens. The non-uniform distribution of {111} density is comparable across all specimens. Note the common absence of {111} density along BD, indicating few grains in these specimens (low volume fractions) oriented with ⟨111⟩ along BD. High {220} and {200} densities along BD indicate many grains in these specimens (high volume fractions) oriented with ⟨110⟩ or ⟨100⟩ along BD. The strength of the ⟨100⟩ fiber texture component compared to the ⟨110⟩ fiber texture component along this direction varies by sample, with E2 (Fig. A.16B) and E3 (Fig. A.16C) in particular having below-average {200} densities and above-average {220} densities along BD. {311} density is largely uniform and comparable across all specimens, indicating no strongly preferred orientations for ⟨311⟩ in these specimens.

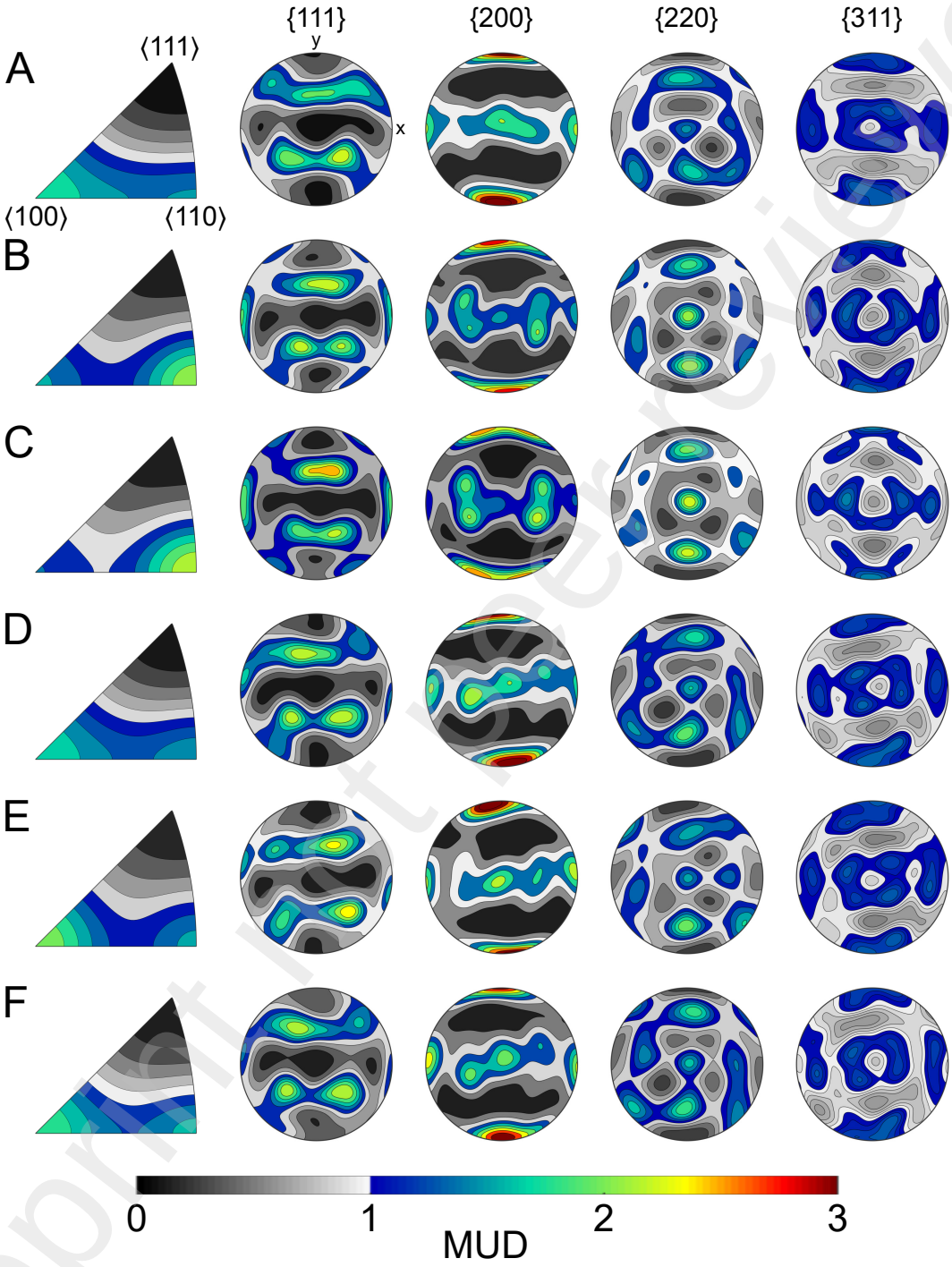

Figure A.16: Orientation distributions represented with inverse pole figures of BD/LD (left) and pole figures (right, BD out-of-plane) in MUD for samples (A-F) E1-E6.

Appendix B. Additional Virtual Microstructures

A third series of simulations was studied to further examine the effects of texture and grain morphology. These 4 microstructures were the same as the P microstructures, but with grain orientations reassigned to eliminate the texture described above. Reassignment was performed by modifying the orientation mapping function used to build ExaConstit meshes from ExaCA voxel data, resulting in a different orientation being assigned to each grain compared to the equivalent P microstructures. With the variation of grain size, this effectively produces random textures. These microstructures will be collectively referred to as the M ("misassigned") microstructures. As these are otherwise the same as the P microstructures, spatial labels of 1-4 are the same as for the P microstructures (Table 2).

One of these microstructures, M1, is shown with IPF-z coloring of the grains in Fig. B.17. The near-random texture is corroborated by the IPF and PFs for this simulated microstructure in Fig. B.18. These display more uniform intensity distributions, lacking any fiber texture components along BD, though some weakly preferred orientations exist away from BD. These preferred orientations vary significantly from microstructure to microstructure and are attributed to grain size effects, i.e., orientations assigned to the large columnar grains vs. the much finer grains between them. These contrast starkly with the strong, consistent textures of the related P microstructures shown in Figs. 6B and 7B.

The macroscopic stress-strain responses of the 4 M microstructures tested at the 3 experimental strain rates are shown in Fig. B.19. Despite having the same grain morphology as the P microstructures, the post-yield ordering of the stress-strain curves is entirely different when comparing the P microstructures to the M microstructures (Fig. 13).

Figures B.20A-D show the evolution of lattice strains along LD with macroscopic strain in the 4 M microstructures for the same fibers as experiment. Again, only the $10^{-3}\,\mathrm{s}^{-1}$ simulations are shown. For these microstructures, the 3 lattice strains showing consistent ordering at yield and post-yield magnitude are ε_{220} (red), then ε_{311} (orange), then ε_{200} (purple), matching what was observed in experiment (Fig. 9) and the P microstructures (Fig. 14). Unlike experiment and the P microstructures, the yield order - but not post-yield magnitude - of ε_{111} was consistent, yielding after ε_{220} and prior to ε_{311} for all microstructures. The post-yield magnitude of ε_{111} was consistent for most microstructures, falling between ε_{220} and ε_{311} for M2, M3, and M4 (Figs. B.20B-D) and following the same hardening behavior as the other lattice strains. M1, however, deviates from this shared post-yield

behavior, as ε_{111} yields after ε_{220} then immediately softens to become the smallest lattice strain, after which it follows the same hardening behavior as the other lattice strains. Like the F microstructures, there is more variability in the post-yield magnitude of ε_{200} compared to experiment or the P microstructures. Like experiment, the variability and unusual hardening/softening behaviors occur in ε_{111} and are independent of strain rate, but, comparable to the P microstructures (Fig. 14), these irregularities are subdued compared to the more extreme behaviors observed in the experimental data (Fig. 9).

In the absence of any fiber texture component along BD/LD and no $\{hkl\}$ density being especially low along BD/LD, these microstructures are functionally a middle ground between the F and P microstructures, reflected in specific behaviors, or a lack thereof, being present from each. In light of these observations, it is perhaps the case that correctly capturing the micromechanical response of this system depends more strongly on specific fiber texture components *not being present* (i.e., the $\langle 111 \rangle$ fiber) rather than specific fiber texture components being present (i.e., the $\langle 110 \rangle$ and $\langle 100 \rangle$ fibers).

Figure B.21 shows the calculated fiber-averaged strength-to-stiffness ratios for the M microstructures. As with the F and P microstructures (Fig. 15), these ratios are relatively consistent across the M microstructures in both order and approximate value despite the differences in texture between them, again with $r_{200} > r_{311} > r_{111} > r_{220}$ corresponding to the common yield order (ε_{220} (red), then ε_{111} (blue), then ε_{311} (orange), then ε_{200} (purple)). The only exception here is M3, for which $r_{111} \approx r_{311}$, though it still has the common yield order. There is again no correlation between unusual lattice strain behaviors and unusual strength-to-stiffness ratios, further supporting the findings described above.

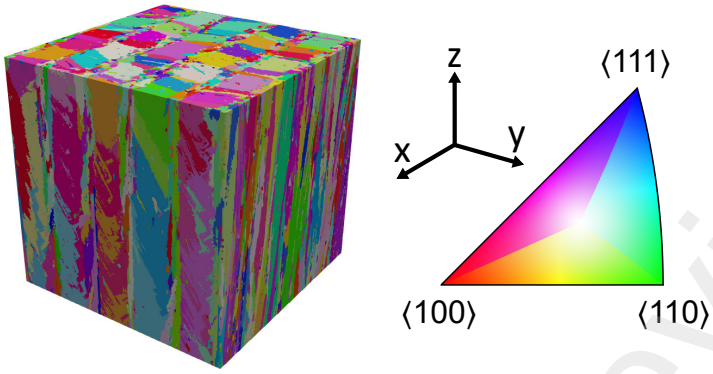

Figure B.17: Simulated microstructure ($0.5 \times 0.5 \times 0.5\,\mathrm{mm}$) M1 with IPF-$z$ coloring, representative of the M microstructures.

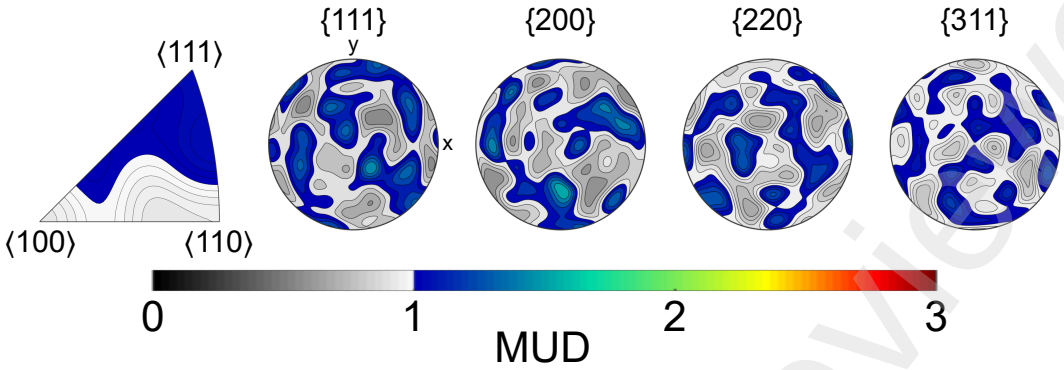

Figure B.18: Orientation distribution represented with inverse pole figures of BD/LD (left) and pole figures (right, BD out-of-plane) for simulated microstructure M1, representative of the M microstructures.

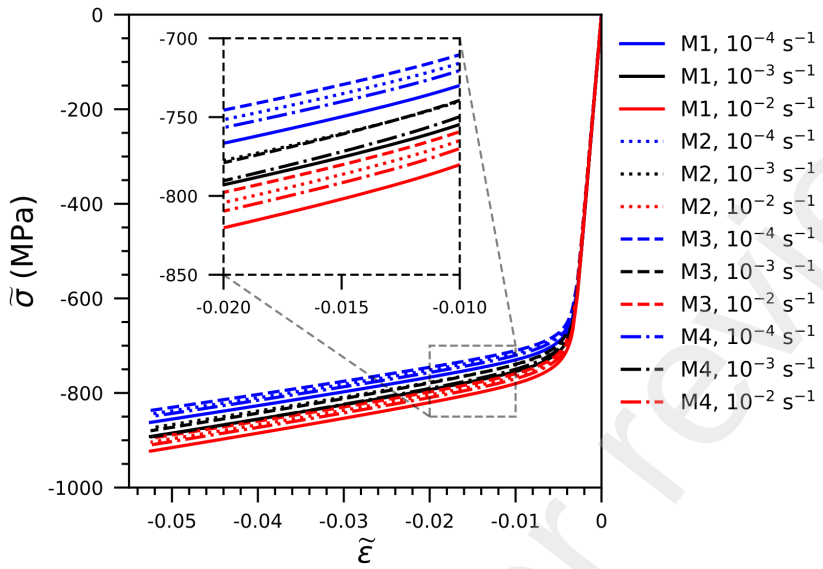

Figure B.19: Macroscopic stress-strain curves for microstructures M1-4, each tested at 3 strain rates (10^{-4}, 10^{-3}, $10^{-2}\,s^{-1}$). Curves are colored by strain rate, with different line styles indicating microstructure ID.

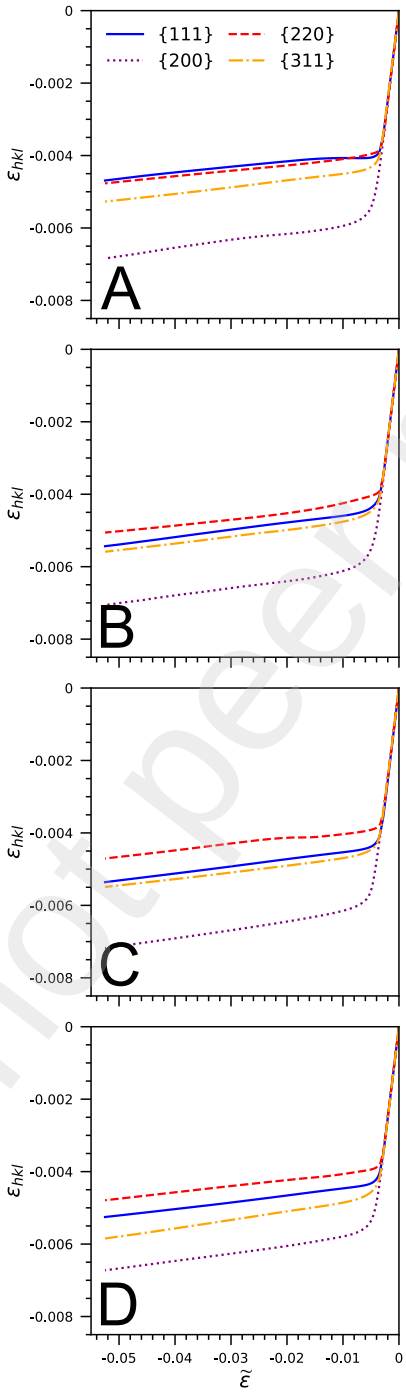

Figure B.20: Lattice strains for microstructures (A-D) M1-4 at $10^{-3}\,\mathrm{s}^{-1}$ strain rate.

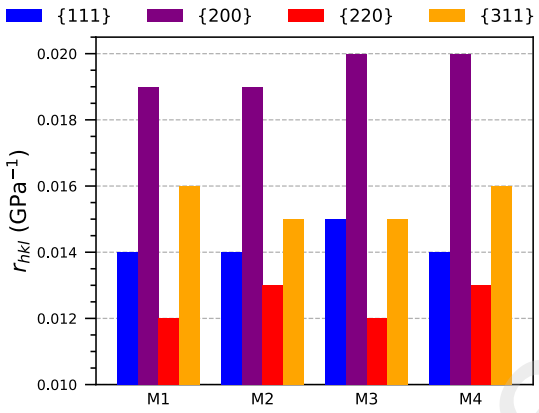

Figure B.21: Directional strength-to-stiffness ratios for the 4 crystallographic fibers examined for the M microstructures.